

# Dearth of dark matter or massive dark halo? Mass-shape-anisotropy degeneracies revealed by NMAGIC dynamical models of the elliptical galaxy NGC 3379

F. De Lorenzi,<sup>1,2\*</sup> O. Gerhard,<sup>2</sup> L. Coccato,<sup>2,3</sup> M. Arnaboldi,<sup>4,5</sup> M. Capaccioli,<sup>6</sup>  
N. G. Douglas,<sup>3</sup> K. C. Freeman,<sup>7</sup> K. Kuijken,<sup>8</sup> M. R. Merrifield,<sup>9</sup> N. R. Napolitano,<sup>6</sup>  
E. Noordermeer,<sup>9</sup> A. J. Romanowsky<sup>3,9,10</sup> and V. P. Debattista<sup>11</sup>

<sup>1</sup>*Astron. Institut, Universität Basel, Venusstrasse 7, Binningen CH-4102, Switzerland*

<sup>2</sup>*Max-Planck-Institut für Ex. Physik, Giessenbachstraße, D-85741 Garching, Germany*

<sup>3</sup>*Kapteyn Astronomical Institute, University of Groningen, Postbus 800, 9700 AV Groningen, the Netherlands*

<sup>4</sup>*ESO, Karl-Schwarzschild-Str. 2, D-85748 Garching, Germany*

<sup>5</sup>*INAF, Observatory of Turin, Strada Osservatorio 20, 10025 Pino Torinese, Italy*

<sup>6</sup>*Osservatorio di Capodimonte, Naples, Italy*

<sup>7</sup>*Research School of Astronomy and Astrophysics, ANU, Canberra, Australia*

<sup>8</sup>*Leiden Observatory, Leiden University, PO Box 9513, 2300RA Leiden, the Netherlands*

<sup>9</sup>*School of Physics and Astronomy, University of Nottingham, University Park, Nottingham NG7 2RD*

<sup>10</sup>*Departamento de Física, Universidad de Concepción, Casilla 160-C, Concepción, Chile*

<sup>11</sup>*Centre for Astrophysics, University of Central Lancashire, Preston PR1 2HE*

Accepted 2009 January 16. Received 2008 December 22; in original form 2007 November 30

## ABSTRACT

Recent results from the Planetary Nebula Spectrograph (PNS) survey have revealed a rapidly falling velocity dispersion profile in the nearby elliptical galaxy NGC 3379, casting doubts on whether this intermediate-luminosity galaxy has the kind of dark matter (DM) halo expected in  $\Lambda$  cold dark matter ( $\Lambda$ CDM) cosmology. We present a detailed dynamical study of this galaxy, combining ground based long-slit spectroscopy, integral-field data from the Spectrographic Areal Unit for Research on Optical Nebulae (SAURON) instrument and PNS data reaching to more than seven effective radii.

We construct dynamical models with the flexible  $\chi^2$ -made-to-measure ( $\chi^2$ M2M) particle method implemented in the NMAGIC code. We fit spherical, axisymmetric and some triaxial models to the photometric and combined kinematic data in a sequence of gravitational potentials whose circular velocity curves at large radii vary between a near-Keplerian decline and the nearly flat shapes generated by massive haloes.

We find that models with a range of halo masses, anisotropies, shapes and inclinations are good representations of the data. In particular, the data are consistent both with near-isotropic systems dominated by the stellar mass and with models in moderately massive haloes with strongly radially anisotropic outer parts ( $\beta \gtrsim 0.8$  at  $7R_e$ ). Formal likelihood limits would exclude (at  $1\sigma$ ) the model with stars only, as well as halo models with  $v_{\text{circ}}(7R_e) \gtrsim 250 \text{ km s}^{-1}$ . All valid models fitting all the data are dynamically stable over gigayears, including the most anisotropic ones.

Overall the kinematic data for NGC 3379 out to  $7R_e$  are consistent with a range of mass distributions in this galaxy. NGC 3379 may well have a DM halo as predicted by recent merger models within  $\Lambda$ CDM cosmology, provided its outer envelope is strongly radially anisotropic.

**Key words:** methods: numerical – galaxies: elliptical and lenticular – galaxies: individual: NGC 3379 – galaxies: kinematics and dynamics.

## 1 INTRODUCTION

There is strong evidence that most galaxies are surrounded by massive dark matter (DM) haloes. This is most evident in spiral galaxies, where the rotation curves of extended cold gas discs remain flat out

\*E-mail: lorenzi@mpe.mpg.de

to large radii. In elliptical galaxies, the evidence for dark haloes has built up more slowly, and their halo properties are not so well known, because of a lack of ubiquitous tracer similar to the H I rotation curves in spirals. Only in a few cases it is possible to measure masses from extended H I ring velocities (e.g. Franx, van Gorkom & de Zeeuw 1994; Oosterloo et al. 2002).

However, at least for giant elliptical galaxies, stellar-dynamical studies from integrated light spectra (e.g. Kronawitter et al. 2000; Gerhard et al. 2001; Cappellari et al. 2006; Thomas et al. 2007), analyses of the X-ray emitting hot gas atmospheres (e.g. Awaki et al. 1994; Matsushita et al. 1998; Loewenstein & White 1999; Fukazawa et al. 2006; Humphrey et al. 2006) and gravitational lensing data (e.g. Wilson et al. 2001; Treu & Koopmans 2004; Rusin & Kochanek 2005; Koopmans et al. 2006; Gavazzi et al. 2007) are now giving a fairly consistent picture. The general result from these studies is that these ellipticals are surrounded by DM haloes, the inferred mass profiles (luminous plus dark) are nearly isothermal, i.e. the circular velocity curves approximately flat, and the DM contributes  $\sim 10$ – $50$  per cent of the mass within  $R_e$ . The central DM densities in ellipticals are higher than in spirals, presumably reflecting their earlier formation epochs (Gerhard et al. 2001; Thomas 2006).

In light of this, the finding of Romanowsky et al. (2003) and Douglas et al. (2007), that several intermediate luminosity ellipticals (NGC 3379, NGC 4494, NGC 821) apparently have only diffuse DM haloes if any, is quite surprising. Could the DM properties of these ellipticals be different from those of giant ellipticals (e.g. Napolitano et al. 2005), perhaps related to the fact that these lower-luminosity galaxies are less often found in groups or clusters? The result of Romanowsky et al. (2003) is based on the outer velocity dispersion profiles of the three galaxies, determined from individual planetary nebulae (PNe) velocities measured with the special PNS instrument (Douglas et al. 2002). Two of the three galaxies are nearly round on the sky, and therefore the dynamical analysis was carried out with spherical models. A fourth galaxy with a fairly rapidly declining outer velocity dispersion profile is NGC 4697 (Méndez et al. 2001). However, using axisymmetric particle models, de Lorenzi et al. (2008) have recently shown that only models with massive dark haloes are consistent with all the kinematic data for this galaxy, and that the best models have circular velocity  $v_c(5R_e) \simeq 250 \text{ km s}^{-1}$  at five effective radii. Unfortunately, the diffuse gas envelopes of these intermediate luminosity ellipticals have very low densities, so an independent confirmation with X-ray data is difficult.

The results of Romanowsky et al. (2003) were criticized by Dekel et al. (2005). These authors pointed out that the well-known mass-anisotropy degeneracy in the study of velocity dispersion profiles does not allow one to unambiguously determine the mass profile, the triaxial nature of elliptical galaxies can cause low line-of-sight velocity dispersions at some viewing angles or the PNe could trace young stars generated during the merger formation instead of the bulk of the old stars as usually assumed. Douglas et al. (2007) argued that Romanowsky et al. (2003) properly took into account orbital anisotropies in the data fitting process, the effect of triaxiality is very unlikely to be present in all three galaxies, the PN number density and velocity dispersion profiles match the corresponding integrated light profiles reasonably well, and this as well as the universality of the bright end of the PN luminosity function rules out that PNe only trace a young stellar population. Douglas et al. (2007) concluded that their results continue to conflict with the presence of DM haloes as predicted in cosmological merger simulations.

The issue is important enough to merit a further careful analysis. In this paper, we construct dynamical models of NGC 3379 with the

very flexible NMAGIC particle code, making use of a variety of kinematic data, including SAURON integral-field data, slit kinematics and the PN dispersion profile.

The NMAGIC method is flexible not only with regard to anisotropy, but also in allowing axisymmetric or triaxial shapes with radially varying axis ratios. This is important since the intrinsic shape of NGC 3379 is still in doubt. Capaccioli et al. (1991) and Statler & Smecker-Hane (1999) have suggested that NGC 3379 is a triaxial S0 galaxy seen almost face-on. Statler (2001) considered triaxial dynamical models and constrained the shape of this galaxy to be axisymmetric and oblate in the inner parts and triaxial in the outer parts. Shapiro et al. (2006) argue that the most likely model is one of a moderately inclined oblate system.

The outline of the paper is as follows. In Section 2, we describe briefly how the various observational data for NGC 3379 are used in the modelling. In Section 3, we give a few details of the  $\chi^2$ M2M NMAGIC method, and show how it performs on a mock galaxy data set similar to that for NGC 3379. In Section 4, we then construct various dynamical models for the real galaxy data, spherical, flattened axisymmetric and triaxial in a sequence of potentials with increasing circular velocity at large radii. As summarized in the final Section 5 of the paper, our main conclusion is that the combined kinematic data for NGC3379 is consistent with a range of DM haloes, including those found by Dekel et al. (2005) in their cosmology-based merger simulations.

## 2 OBSERVATIONAL DATA

We begin by describing the observational data used in this study, which are all taken from the literature. We also describe here the procedure employed for obtaining the three-dimensional luminosity density from the surface brightness (SB) data. In the following, we adopt a distance 9.8 Mpc to NGC 3379 (Jensen et al. 2003), effective radius  $R_e = 47 \text{ arcsec}$  (2.23 kpc) and an absolute  $B$  magnitude  $M_B = -19.8$  (Douglas et al. 2007).

### 2.1 Photometric data

The photometric data used in the present work consists of the ground-based wide-field  $B$ -band photometry of Capaccioli et al. (1990), combined with the *Hubble Space Telescope* (HST)  $V$ -band observations of Gebhardt et al. (2000) to increase the spatial resolution within the inner 10 arcsec. The photometry has been matched up by assuming a constant colour offset  $B - V = 1.03$ . The last eight SB points from Capaccioli et al. (1990), outside  $R \simeq 500 \text{ arcsec}$ , show fluctuations of an amplitude which we judged unphysical; these points we have replaced with a Sersic (1968) profile fitted to the galaxy further in. The same Sersic fit is used to extrapolate the SB profile outside the last measured point at  $R = 676 \text{ arcsec}$ . Similarly, we have replaced the measured ellipticities for  $R > 81 \text{ arcsec}$ , where the observational uncertainties become large by  $\epsilon = 0.14$ . Fig. 1 presents the combined photometric data, showing SB and ellipticity  $\epsilon$ . The isophotal shape parameters  $a_4$  and  $a_6$  are not available for these data and are thus set to zero. For the spherical models, we have used the SB profile rescaled to a mean radius  $R_m \equiv \sqrt{ab} = a\sqrt{1 - \epsilon}$ . For the axisymmetric models, we have used a constant position angle (PA) of  $70^\circ$ ; the isophotal PA measured by Capaccioli et al. (1990) are within  $\pm 3^\circ$  of this value.

### 2.2 Deprojection

In our implementation of NMAGIC, a particle model can be fitted to the SB and/or the deprojected luminosity density (cf. Section 3).

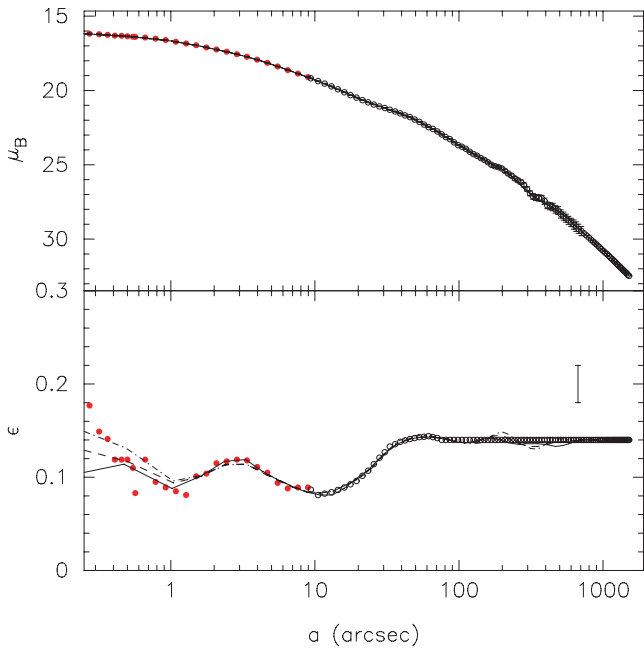


**Figure 1.** Combined photometry of NGC 3379 from Capaccioli et al. (1990) (open black circles) and Gebhardt et al. (2000) (full red circles). The two panels show the surface brightness (SB) profile and the ellipticity  $\epsilon$  as a function of major axis distance. Beyond 500 arcsec the SB points are from a Sersic model fitted to the interior data, and outside 81 arcsec, the ellipticity has been set to  $\epsilon = 0.14$ . In the ellipticity panel, the error bar with size 0.02 illustrates the typical errors in the outer ellipticity measurements. The isophotal shape parameters  $a_4$  and  $a_6$  are not measured; they are set to zero. The lines show three-dimensional luminosity models determined from these data and reprojected on to the sky, for assumed inclinations of  $i = 90^\circ$  (edge-on, full lines),  $i = 50^\circ$  (dashed lines) and  $i = 40^\circ$  (dash-dotted lines).

Below we use both options, so first need to construct models for the three-dimensional luminosity density,  $j$ .

In the spherical case, the SB can be deprojected uniquely. For an axisymmetric system the deprojection is unique only for edge-on galaxies; for systems inclined at an angle  $i$  with respect to the line of sight, the SB map contains information about the luminosity density only outside a ‘cone of ignorance’ in the Fourier space, of opening angle  $90^\circ - i$ , when  $i = 90^\circ$  denotes edge-on (Rybicki 1987). Thus, the deprojection of a moderately inclined galaxy results in undetermined konus densities (Gerhard & Binney 1996; Romanowsky & Kochanek 1997).

We deproject the SB of NGC 3379, without correcting for point-spread function (PSF) effects, using the program of Magorrian (1999). The program finds a smooth axisymmetric density distribution consistent with the SB distribution for the specified inclination angle, by imposing that the solution maximizes a penalized likelihood. This ensures that the shape of the three-dimensional luminosity density is smooth and biases the model towards a specified disciness, measured by the  $\cos 4\theta$  Fourier coefficient (cf. Magorrian 1999). Because of the disc-like nature of the undetermined konus densities, requesting the luminosity density to have zero disciness effectively chooses between the different density distributions that fit the SB data for  $i \neq 90^\circ$ . We have used the program to compute luminosity densities for NGC 3379 for the inclinations  $i = 90^\circ$ ,  $i = 50^\circ$  and  $i = 40^\circ$ ; more face-on axisymmetric luminosity densities are disc-like or not consistent with the photometry. Fig. 1 compares

the observed photometry with the three deprojections reprojected on to the sky.

## 2.3 Kinematic data

### 2.3.1 Stellar-absorption line data

We have taken long-slit absorption line kinematics from the literature. We use data from Statler & Smecker-Hane (1999) at four different position angles, extending out to radii of  $\approx 80$  arcsec. We complement these kinematics with the spectroscopic data from Kronawitter et al. (2000). The major axis slits from Statler & Smecker-Hane (1999) and Kronawitter et al. (2000) are misaligned by  $10^\circ$  in PA; however, the data along both major axis slits follow each other closely. The measurements along the shifted slit of Kronawitter et al. (2000) reach 100 arcsec from the centre. From both kinematic data sets, we have the line-of-sight velocity, velocity dispersion and higher order Gauss–Hermite moments  $h_3$  and  $h_4$  (Gerhard 1993; van der Marel & Franx 1993). Fig. 2 shows the schematic arrangement of the kinematic slits used in the dynamical modelling.

In addition to the long-slit kinematics, we also use the integral-field spectroscopy obtained with the SAURON instrument. These kinematic data were kindly provided by Shapiro et al. (2006) and consist of line-of-sight velocity, velocity dispersion and higher order Gauss–Hermite moments up to  $h_6$ . The SAURON field-of-view (FoV), shown by the (blue) rectangle in Fig. 2, extends from  $-19.6$  to  $24.4$  arcsec along its short boundary and from  $-34.8$  to  $35.6$  arcsec along the long boundary. In this FOV, the positions of the

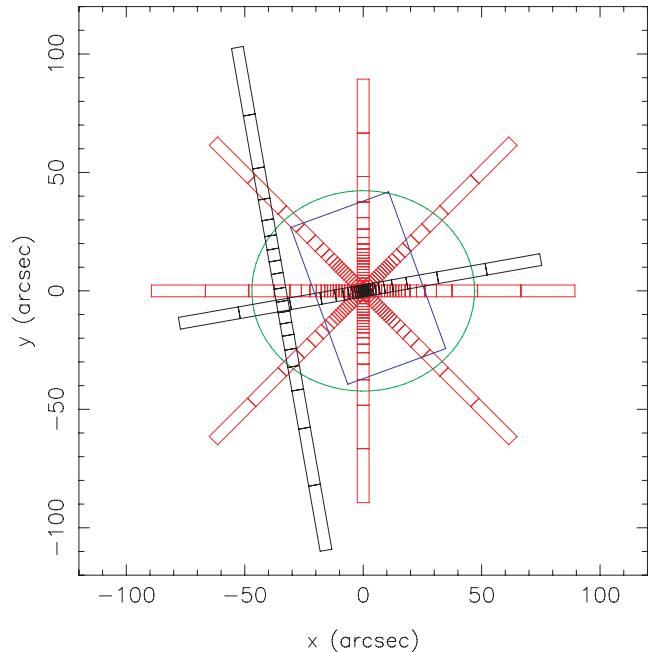


**Figure 2.** Schematic view of the positions with kinematic data as used to construct the dynamical models. The slits from Statler & Smecker-Hane (1999) and Kronawitter et al. (2000) are coded in red and black, respectively. Boxes along the slits show the region of the galaxy for which respective kinematic data points were derived; these boxes are used to determine the luminosity-weighted Gauss–Hermite moments. The blue rectangle indicates the SAURON FoV. The ellipse shown is oriented along PA =  $70^\circ$ , the average major axis of the photometry and has a semimajor axis of length  $R_c$  and axis ratio  $q = 0.9$ .

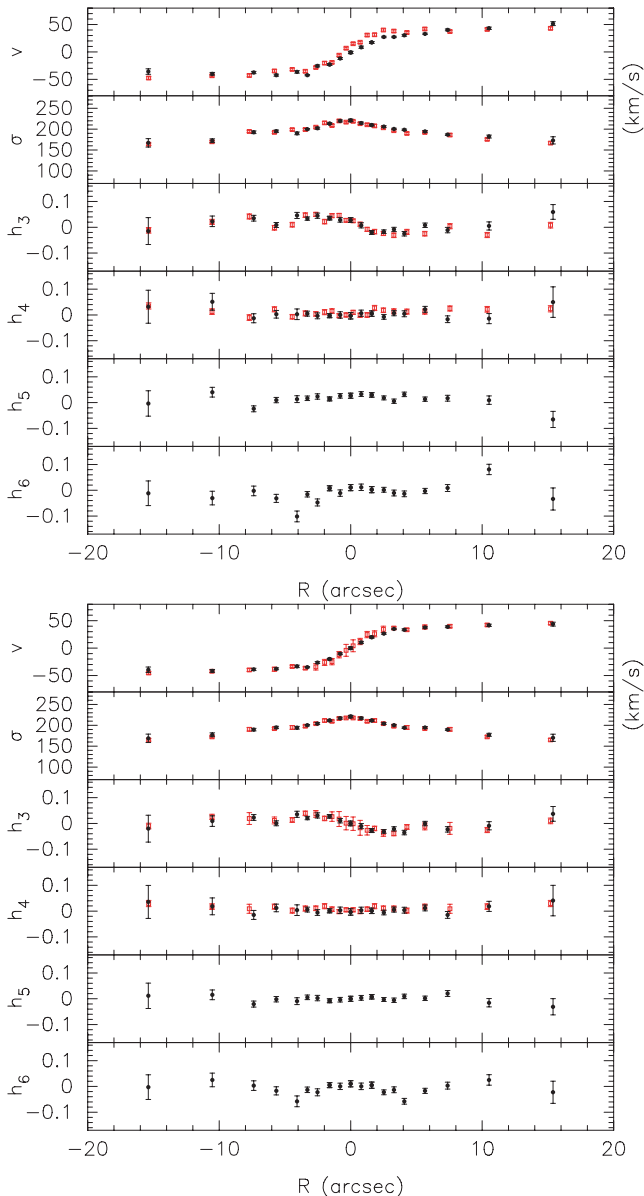


**Figure 3.** Comparison of the line-of-sight velocity distribution data along the galaxy’s major axis ( $PA = 70^\circ$ ). The black circles correspond to the SAURON data and the open square symbols in red show the Kronawitter et al. (2000) data. The upper panel compares the original data sets, the lower panel is for the symmetrized data. In each panel from top to bottom are shown:  $v$ ,  $\sigma$ ,  $h_3$ ,  $h_4$ ,  $h_5$  and  $h_6$ , for the latter two there are only SAURON data.

$55 \times 88$  ‘lenslets’ with which spectra were taken define a fine grid of 4840 grid cells, which serve as the basis grid to define the 1602 voronoi cells on which the final kinematic measurements are given. This results in a total of 9612 kinematic SAURON observables, as well as 1602 bin-luminosity observables. The SAURON data are reproduced and compared to dynamical models in Section 4. Each of the six panels shows the 1602 voronoi bins, giving (from left to right)  $v$ ,  $\sigma$ ,  $h_3$ ,  $h_4$ ,  $h_5$  and  $h_6$ . A comparison of the SAURON data with the data of Kronawitter et al. (2000) along their major axis is given in Fig. 3. Overall, the two data sets agree well with each other. The same is true for the comparison of the SAURON data with Statler & Smecker-Hane (1999), as shown by Shapiro et al. (2006).

Both the SAURON data and the slit data are slightly asymmetric with respect to the centre of the galaxy. If we denote the original SAURON data set with  $I(x, y|v_{\text{los}}, \sigma_{\text{los}}, h_3, h_4, h_5, h_6)$  and with  $I^*(x, y|v_{\text{los}}, \sigma_{\text{los}}, h_3, h_4, h_5, h_6) = I(-x, -y, |-v_{\text{los}}, \sigma_{\text{los}}, -h_3, h_4, -h_5, h_6)$ , the data set obtained from  $I$  by point-symmetrical reflection with respect to the origin, we can construct a symmetrized data set  $\bar{I} \equiv 0.5(I + I^*)$ . This symmetrized data set  $\bar{I}$  has a  $\chi^2$  per data point with respect to  $I$  of  $\chi^2/N = 1.01$  when the original errors are used. Any point-symmetric model fit (spherical, axisymmetric, triaxial) to the original data  $I$  will therefore have a systematic error floor of this magnitude. In the models below, we will actually fit the symmetrized SAURON data to avoid any systematic effects, but keep the original errors on both sides of the galaxy separately (see also Shapiro et al. 2006).

In a similar fashion, we have constructed symmetrized slit data sets. To do this, we average the two points at nearly similar radii on both sides of the slit with respect to the centre. Taking into account the sign reversals of  $v$  and  $h_3$ , we take for the symmetrized data point the weighted mean of the points on both sides, with weights proportional to the inverse square of the measurement errors, and assign a new weighted error for the averaged point. If  $\sigma_+$  and  $\sigma_-$  are the errors on both sides, the weights are  $w_+ = 1/\sigma_+^2$ ,  $w_- = 1/\sigma_-^2$ , and the new error  $\sigma$  is given by the maximum of  $2/\sigma^2 = 1/\sigma_+^2 + 1/\sigma_-^2$  and half of the deviation between the original data points on both sides. Again, the symmetrized data have a  $\chi^2/N = 1.0$  systematic deviation from the original data, and therefore we will fit the symmetrized data below to avoid the model being pulled around by points with small error bars but large systematic deviations. The second panel of Fig. 3 compares the symmetrized SAURON data with the symmetrized Kronawitter et al. (2000) data along the same slit as before. Again, the two data sets agree well with each other.

### 2.3.2 PNe data

PNe are dying low-to-intermediate mass stars that emit most of their light in a few narrow lines of which the  $[\text{OIII}]\lambda 5007$  is the most prominent one. The PN population in elliptical galaxies is expected to arise from the underlying galactic population of old stars. Because there are hardly any other emission sources in elliptical galaxies, PNe can be detected fairly easily and their line-of-sight velocities measured from the Doppler shifted emission line. Hence, PNe are excellent kinematic tracers for the stellar distribution at radii where the SB is too faint for absorption line spectroscopy.

Douglas et al. (2007) processed observations of NGC 3379 conducted with the Planetary Nebula Spectrograph (PNS) instrument and detected 214 spatially and spectrally unresolved PN candidates of which 191 are assigned to NGC 3379. Using the ‘friendless’ algorithm applied by Merrett et al. (2003), they identified a small number of velocity outliers, probably unresolved background galaxy contaminants, which would be uniformly spread in velocity. The algorithm determined that two emission objects were more than  $n = 5$  standard deviations away from the centroid of the velocity distribution of their  $N = 15$  nearest neighbours, and three objects more than 3 standard deviations  $\sigma$  (see fig. 8 of Douglas et al. 2007). The  $3\sigma$  line itself has considerable uncertainty at large radii due to the small number of PNe found there. Thus, the exclusion of the outermost outlier is somewhat uncertain. Because this object does have some influence on the outermost velocity dispersion point, we will compare the models to the data obtained both with and without this PN.

The radial distribution of the PNe in the final NGC 3379 sample of Douglas et al. (2007) is consistent with the stellar density profile, and their kinematics is consistent with absorption-line data in the region where the data sets overlap (see their figs 6 and 7 and Coccato et al. 2009). Because the kinematics of the PNe in NGC 3379 are dominated by random motions with little azimuthal variation, the velocity dispersion can be computed in radial annuli without losing significant dynamical structure. We will thus use the radial run of the azimuthally averaged PN velocity dispersion in the dynamical modelling, but also compare the models to the individual velocities in a relative likelihood sense (cf. the tables and figures in Section 4).

### 3 NMAGIC MODELLING

To investigate the amount of DM consistent with the kinematic data for NGC 3379, we construct a range of dynamical models for the stellar component of this galaxy. We use the flexible  $\chi^2$ M2M particle method as described and implemented in the NMAGIC code by de Lorenzi et al. (2007), de Lorenzi et al. (2008).  $\chi^2$ M2M is a development of the M2M algorithm of Syer & Tremaine (1996) that is suitable for modelling observational data. The M2M methods work by gradually adjusting individual particle weights as the model evolves, until the  $N$ -particle system reproduces a set of target constraints. In  $\chi^2$ M2M, the standard  $\chi^2$  statistics is used in the function to be maximized upon convergence of the weights. This allows for a proper treatment of observational errors, and the quality of the final model can be assessed directly from the target data.

Compared to the familiar Schwarzschild method (e.g. Schwarzschild 1979; Rix et al. 1997; van der Marel et al. 1998; Cretton et al. 1999; Romanowsky & Kochanek 2001; Gebhardt et al. 2003; Thomas et al. 2004; Valluri, Merritt & Emsellem 2004; Cappellari et al. 2006; Chanamé, Kleyna & van der Marel 2008; van den Bosch et al. 2008), the particle approach is relatively new and there are as yet only a few galactic dynamics studies in which it has been employed. Bissantz, Debattista & Gerhard (2004) made a first practical application of the M2M method of Syer & Tremaine (1996) and constructed a dynamical model of the Milky Way's barred bulge and disc by constraining the projected density map. First attempts to extend the M2M method to account for kinematic observables in addition to density constraints were made by de Lorenzi, Debattista & Gerhard (2006) and Jourdeuil & Emsellem (2007). However, a proper treatment of observational errors was not yet included in their implementations. de Lorenzi et al. (2007) incorporated this in their  $\chi^2$ M2M algorithm and demonstrated the potential of the NMAGIC code by constructing particle models for spherical, axisymmetric, triaxial and rotating target stellar systems. Some extensions of the method and the first detailed modelling of slit kinematic and PN data for an elliptical galaxy (NGC 4697) are described in de Lorenzi et al. (2008).

The NMAGIC method is flexible not only with regard to the orbit structure, but also in allowing axisymmetric or triaxial shapes with varying axis ratios. Contrary to Schwarzschild's method, the 'best' stellar density and luminous potential need not be specified beforehand, but can be found from the evolution of the model. This makes it ideal for the present study because different intrinsic shapes have been suggested for NGC 3379 (see the Introduction), and the issue of whether the kinematics require or allow DM may well be connected not only with the orbital anisotropies but also with the detailed shape of the stellar density distribution of the galaxy. Given that NGC 3379 is nearly round on the sky, we have constrained most models in this paper to be spherical or axisymmetric, with density distribution fixed from the deprojection; however, for some models

(in Sections 4.2.1 and 4.3), we let the stellar system evolve towards a final 'best', weakly triaxial density distribution allowing for radial variations in axis ratio. This approach has proved sufficient for answering our main science question.

#### 3.1 Luminous and dark mass distributions

As in de Lorenzi et al. (2008), we assume that the luminous mass of NGC 3379 follows the light and characterize it by a constant mass-to-light ratio  $\Upsilon$ , so that the stellar mass density is given by  $\rho_* = \Upsilon j$ . The total gravitational potential is generated by the combined luminous mass and DM distributions,  $\phi = \phi_* + \phi_L$ , where  $\phi_*$  is generated by  $\rho_* = \Upsilon j$ . Only the luminosity density  $j$  is represented by the  $N$ -particle system. Its potential is computed using a spherical harmonic decomposition as described in Sellwood (2003) and de Lorenzi et al. (2007). The stellar potential is allowed to vary during the modelling process, but the DM halo is spherical and rigid throughout.

Here, our aim is not to determine the detailed shape of the DM halo in NGC 3379, but rather to first see whether the PN velocities allow or require any DM at all in this galaxy. To answer this question, we will investigate a one-dimensional sequence of potentials whose circular velocity curves vary at large radii between the near-Keplerian decline expected when the mass in stars dominates, and the nearly flat shapes generated by massive dark haloes. As in de Lorenzi et al. (2008), we thus represent the DM halo by the logarithmic potential (Binney & Tremaine 1987):

$$\phi_L(r) = \frac{v_0^2}{2} \ln(r_0^2 + r^2). \quad (1)$$

#### 3.2 Model and target observables

Target observables include surface or volume densities and line-of-sight kinematics. For modelling the luminosity distribution of NGC 3379, we generally use the deprojected luminosity density of NGC 3379, expanded in spherical harmonic coefficients  $A_{lm}$  on a one-dimensional radial mesh of radii  $r_k$ . The corresponding model observables are computed from the particles based on a cloud-in-cell (CIC) scheme (see de Lorenzi et al. 2007).

In some models, we do not constrain the three-dimensional luminosity density but only the stellar surface density, leaving the former free to evolve. In other cases, we constrain the model by both the deprojected luminosity density and the projected surface density. In a similar spirit as for the volume density, we use as target constraints for the observed SB distribution the coefficients of a Fourier expansion in the azimuthal angle, computed on a one-dimensional radial mesh of projected radii  $R_k$ . For the corresponding model observables, the particles are assigned to the radial grid using a CIC scheme, and the Fourier coefficients  $a_m$  and  $b_m$  for the particle model on shell  $k$  are computed via

$$a_{m,k} = L \sum_i \gamma_{ki}^{\text{CIC}} \cos(m\varphi_i) w_i, \quad (2)$$

$$b_{m,k} = L \sum_i \gamma_{ki}^{\text{CIC}} \sin(m\varphi_i) w_i, \quad m > 0, \quad (3)$$

where  $w_i$  are the particle weights,  $\varphi_i$  their angular positions and  $\gamma_{ki}^{\text{CIC}}$  is a radial selection function. We use units for which the light  $L_i$  of a stellar particle can be written as  $L_i = L w_i$  with  $L$  the total luminosity of the galaxy.

As kinematic constraints, we use the luminosity-weighted Gauss–Hermite coefficients from the SAURON or slit data, and luminosity-weighted velocity moments for the PN data. For the SAURON data (Shapiro et al. 2006), the luminosity-weighted coefficients are determined from the truncated Gauss–Hermite representation of the line-of-sight velocity distribution (LOSVD) up to order  $h_6$  and the luminosity in the corresponding Voronoi bin. For the slit data (Statler & Smecker-Hane 1999; Kronawitter et al. 2000), they are constructed again from the measured Gauss–Hermite moments, up to order  $h_4$ , and the luminosity in the slit section corresponding to the relevant LOSVD. The PN data (Douglas et al. 2007) are modelled either as one-dimensional radial dispersion profile or as a discrete set of velocities; in the former case, we use as suitable observables the second velocity moments  $v_{\text{los}}^2$ , luminosity-weighted by the number of PNe per radial bin.

The corresponding model observables  $y_j$  are constructed from the particles via equations of the form

$$y_j(t) = \sum_{i=1}^N w_i K_j [z_i(t)], \quad (4)$$

where  $w_i$  are the particle weights and  $z_i$  are the phase-space coordinates of the particles and  $i = 1, \dots, N$ . Here, the Kernel  $K_j$  corresponds to the observable  $y_j$ . Detailed expressions for the kinematic model observables are given in de Lorenzi et al. (2007), de Lorenzi et al. (2008).

In general, we replace the observables by the corresponding temporally smoothed quantities to increase the effective number of particles in the system (cf. Syer & Tremaine 1996; de Lorenzi et al. 2007). For the parameters chosen, the smoothing is typically over  $\sim 10^3$  correction time steps.

### 3.3 Constructing a particle model for the target data

Generating an NMAGIC model for a set of observational constraints proceeds by evolving the force-of-change (FOC) equations for the particle weights,

$$\frac{dw_i(t)}{dt} = \varepsilon w_i(t) \left\{ \mu \frac{\partial S}{\partial w_i} - \sum_j \frac{K_j [z_i(t)]}{\sigma(Y_j)} \Delta_j(t) \right\}, \quad (5)$$

depending on the discrepancies between model ( $y_j$ ) and target observables ( $Y_j$ ),  $\Delta_j(t) = (y_j - Y_j)/\sigma(Y_j)$ . Here,  $\sigma(Y_j)$  in the denominator is the error in the target observable. Evolving the particle weights to convergence in this way is equivalent to maximizing the merit function

$$F = \mu S - \frac{1}{2} \chi^2 \quad (6)$$

with respect to the particle weights  $w_i$ , where for the profit function  $S$  we use the entropy, and the standard  $\chi^2$  measures the goodness of the fit. The parameter  $\mu$  controls the contribution of the entropy function to  $F$ . The entropy term pushes the particle weights to remain close to their priors, so models with large  $\mu$  will have smoother distribution functions (DFs) than those with small  $\mu$ . The best choice for  $\mu$  depends on the observational data to be modelled, e.g. spatial coverage and phase-space structure of the galaxy under consideration, but also on the initial conditions, and will be determined for the NGC 3379 data set in Section 3.4.

Any NMAGIC model starts from a suitable initial model. For the models presented in this paper, we have used as initial conditions a Hernquist (1990) model particle realization generated from a DF using the method described in Debattista & Sellwood (2000). The particle realization consists of  $7.5 \times 10^5$  particles, has a scale length

$a = 1$ , maximum radius  $r_{\text{max}} = 60$  and a total luminosity and mass-to-light ratio of unity. In model units, the gravitational constant is  $G = 1$ . In real units, the model length scale corresponds to 50 arcsec. Thus, when we match the model to NGC 3379, the effective radius of NGC 3379 becomes 0.94 model units or 2.23 kpc at a distance of 9.8 Mpc.

### 3.4 Anisotropic mock galaxy model

To prepare for the modelling of NGC 3379, we now construct a spherical mock galaxy model with known intrinsic properties to determine the optimal value of the entropy ‘smoothing’ parameter  $\mu$  in equation (6). Following a similar approach as in Gerhard et al. (1998) and Thomas et al. (2005), we determine for which value of  $\mu$  the fitted particle model best reproduces the intrinsic velocity moments of the input mock galaxy model. The ‘best’ value of  $\mu$  depends on the observational data to be modelled and their spatial coverage, on the phase-space structure of the galaxy, but also on the initial conditions from which the NMAGIC modelling starts. The same value can then be used for the modelling of NGC 3379, provided the mock galaxy is a reasonable approximation to the real galaxy.

For the luminosity density of the mock galaxy, we use a Hernquist (1990) model with total luminosity  $L = 1.24 \times 10^{10} L_{\odot,B}$  and scale radius  $a = 0.8$  kpc, corresponding to  $R_e \approx 30$  arcsec for the distance of NGC 3379. As Fig. 4 shows, the SB profile of this model galaxy is a good approximation for NGC 3379.

For the DF of the mock galaxy, we take an Osipkov–Merritt model (Osipkov 1979; Merritt 1985) with anisotropy radius  $r_a = 9a$ , giving an anisotropy profile similar to some of our later models for NGC 3379. The LOSVD kinematics is calculated following Carollo, de Zeeuw & van der Marel (1995) and setting the mass-to-light ratio to  $\Upsilon_B = 5$ . To the final LOSVD parameters, we add the Gaussian random variates with  $1\sigma$  dispersions equal to the respective error bars of the corresponding NGC 3379 measurements at that point. In this way, we compute  $v$ ,  $\sigma$ ,  $h_3$  and  $h_4$  points for the mock galaxy along all slits shown in Fig. 2. Fig. 5 compares the kinematics of NGC 3379 with the mock galaxy model along the major axis.

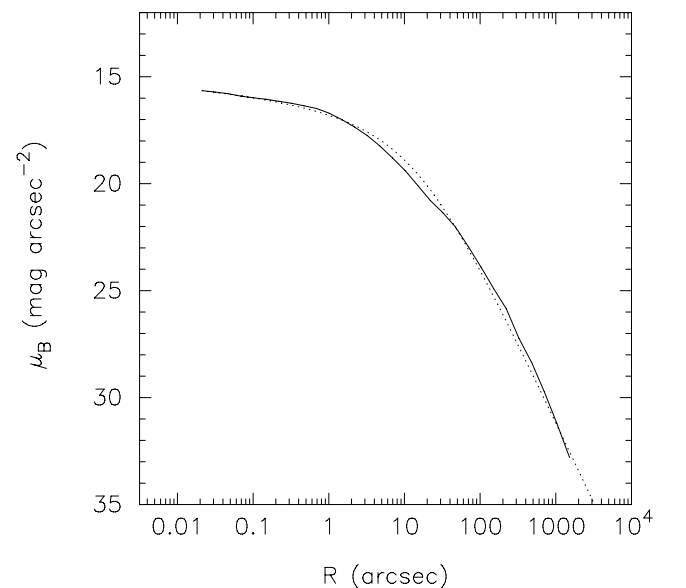


**Figure 4.** A comparison of the surface brightness profile of the mock galaxy model (dotted line) with that of NGC 3379 (full line) along the major axis of NGC 3379.

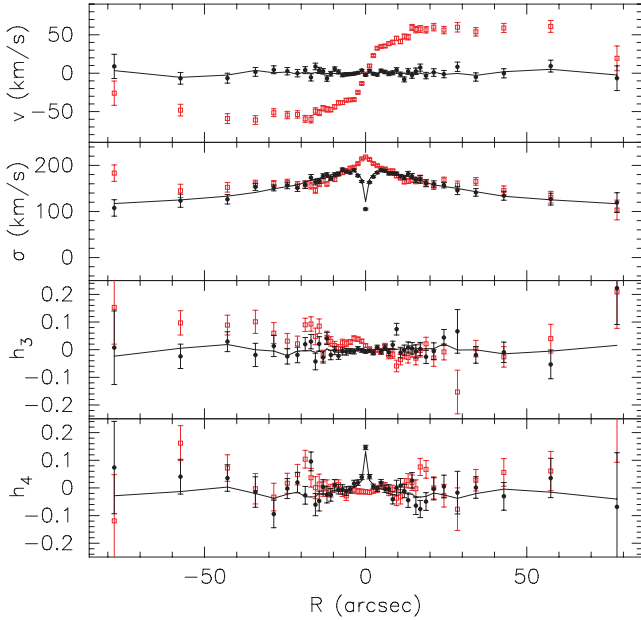


**Figure 5.** Comparison of the LOSVD kinematics of the mock galaxy model with those of NGC 3379 along its major axis and with the particle model fit for  $\mu = 2 \times 10^3$ . The red open squares show the NGC 3379 data from Statler & Smecker-Hane (1999), the black circles show the pseudo data and the solid line the self-consistent particle model obtained from fitting the pseudo data. The model data points are averages over the slit cells (see Fig. 2) and are connected by straight line segments. The panels from top to bottom are for  $v$ ,  $\sigma$ ,  $h_3$  and  $h_4$ .

In addition, we construct SAURON mock kinematics for each voronoi cell in the NGC 3379 data as follows. We first compute the velocity profiles as above at a few nearby radial positions. Using the spherical symmetry, we interpolate  $v$ ,  $\sigma$  and the higher order moments to the mid-cell positions of the fine grid described in Sec-

tion 2.3 using a spline interpolation scheme. Then, we compute the mock data for each voronoi bin by a luminosity weighted average over those cells of the fine grid which contribute to the voronoi cell under consideration. Finally, we add the Gaussian random variates to the kinematics with  $1\sigma$  dispersions corresponding to the respective SAURON error bars in this voronoi bin. The SAURON pseudo data are shown in the top panels of Fig. 6.

The kinematic data set is completed with mock PN dispersion data, using the projected velocity dispersions from Carollo et al. (1995) and the errors from the observed PN dispersion points in NGC 3379. For test purposes, we also use two other sets of mock PN data with smaller errors (see Fig. 7). Again, the Gaussian random variates corresponding to these errors are added to account for the scatter in the velocity dispersion points. Finally, we complete the mock observational data set with the photometric constraints. In the entropy tests here, we restrict ourselves to spherical models, so in the expansion of the luminosity density the only non-zero term in the spherical harmonics series (cf. Section 3.2) is the radial light in shells,  $L_k = \sqrt{4\pi}A_{00,k}$ . However, to ensure sphericity, we also need to use the higher order coefficients  $A_{20,k}, \dots, A_{22,k}$  and  $A_{66,k}$  as constraints, set to zero. We define these photometric observables on a grid of radii  $r_k$ , quasi-logarithmically spaced in radius with inner and outer boundaries at  $r_{\min} = 0.01$  arcsec and  $r_{\max} = 2500$  arcsec. We assume Poisson errors for the radial light  $\sigma(L_k) = \sqrt{L_k L/N}$  where  $N$  is the total number of particles used in the particle model and  $L$  is the total light of the system. To estimate the errors in the higher order luminosity moments, we use Monte Carlo experiments in which we compute the  $A_{lm}$  many times from random rotations of a particle realization of the target density distribution. In these experiments, the number of particles is  $7.5 \times 10^5$ , which is the same number as in the  $\chi^2$ M2M models.

We now construct self-consistent particle models for the anisotropic model galaxy target in a two-step process, using the mock observations as constraints for NMAGIC. First, we start with the particle model described in Section 3.3 and evolve it using NMAGIC to generate a self-consistent particle realization with the

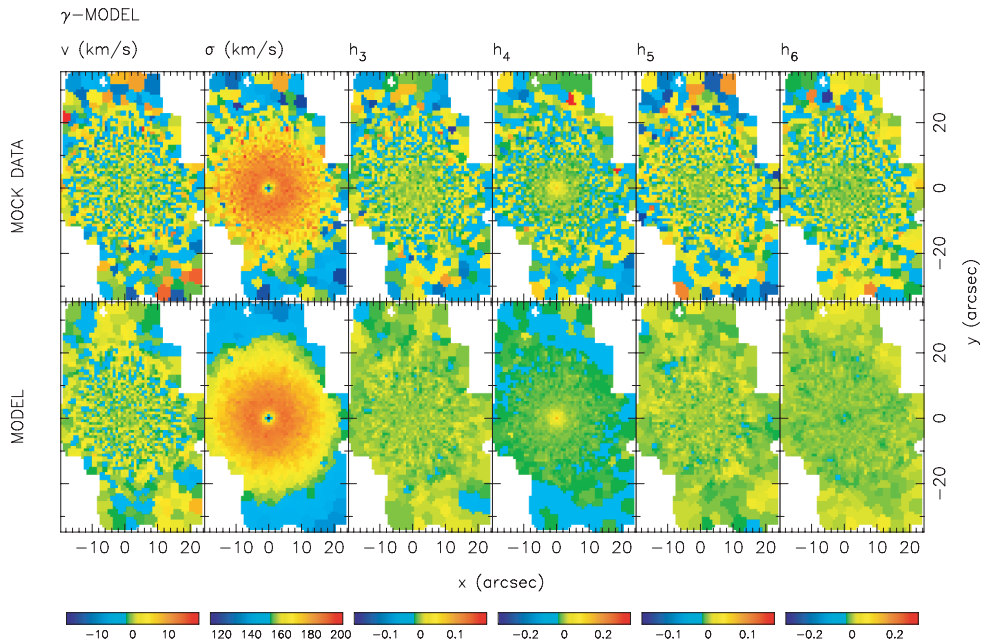


**Figure 6.** Top panel: SAURON mock kinematic data for an anisotropic spherical galaxy model. Bottom panel: self-consistent particle realization obtained from a model fit with  $\mu = 2 \times 10^3$ . From left to right:  $v$ ,  $\sigma$  and the higher order moments  $h_3$ – $h_6$ .

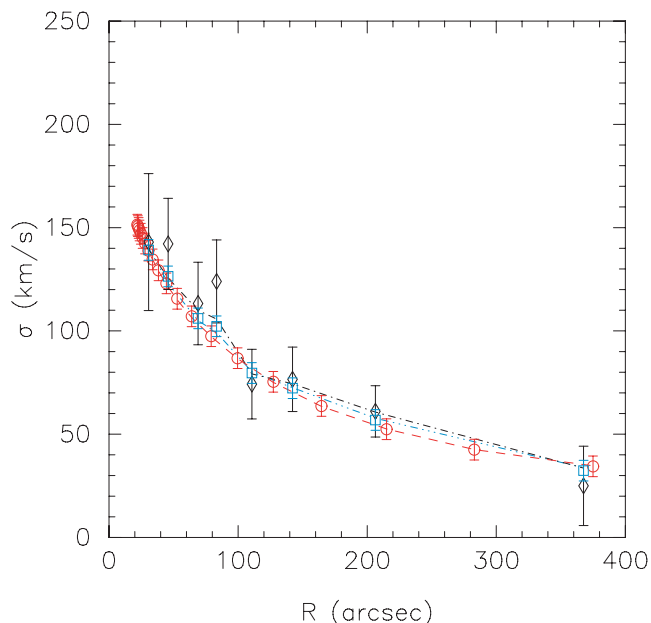
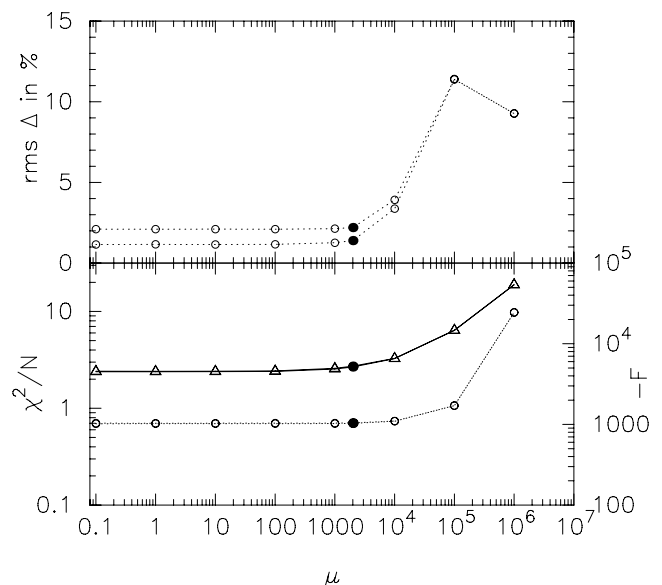


**Figure 7.** Different mock PN velocity dispersion data for the anisotropic spherical target galaxy model and corresponding model velocity dispersion profiles obtained with  $\mu = 2 \times 10^3$ . The three mock data sets differ by the quality with which they represent the underlying target velocity dispersion profile. The black diamonds have been obtained using the original errors of the Douglas et al. (2007) PNe velocity dispersion data. The blue squares show the data obtained using reduced errors of  $5 \text{ km s}^{-1}$  and the red circles illustrate an idealized data set with an increased radial resolution. The corresponding *NMAGIC* models are presented by the black dash–dotted line, the blue dash–dot–dot–dot line and the red dashed line, respectively. The latter is indistinguishable from the target velocity dispersion profile.

desired luminosity distribution (mock particle model), fitting only the photometric constraints. Then, we use the mock particle model as initial conditions to fit both the kinematic and photometric target constraints for different values of  $\mu$ .

The results are presented in Fig. 8. The lower panel shows the goodness of the fit as a function of  $\mu$ , both in terms of the normalized  $\chi^2$  per data point and in terms of the merit function  $F$  from equation (6). The upper panel shows the rms relative difference  $\Delta$  between the true internal velocity moments of the mock galaxy and those of the particle model realizations obtained for different values of  $\mu$ . The intrinsic kinematics of the particle models are computed by binning the particles in spherical polar coordinates, using a quasi-logarithmic grid with 21 radial shells bounded by  $r_{\min} = 0.01$  and  $r_{\max} = 500.0$  arcsec, 12 bins in azimuthal angle  $\phi$  and 21 bins equally spaced in  $\sin\theta$ . As can be seen from the top panel of Fig. 8, there is no minimum in the rms  $\Delta$  as a function of  $\mu$ , but the particle models recover the internal moments of the input model well for  $\mu \lesssim 2 \times 10^3$ . For larger  $\mu$ , the rms  $\Delta$  increases rapidly because of oversmoothing in the model. The lower panel of the figure shows that  $\chi^2$  per data point is below unity for a large range of  $\mu$  but then increases for  $\mu \gtrsim 2 \times 10^3$ . In our modelling of NGC 3379 below, we have confirmed that this value of  $\mu$  allows the models to converge towards strongly anisotropic orbit distributions. We have therefore used  $\mu = 2 \times 10^3$  in Section 4 throughout. This is indicated by the solid symbol in Fig. 8.

Figs 5, 6 and 7 compare the anisotropic mock galaxy model and the particle model obtained from the target data with  $\mu = 2 \times 10^3$ .



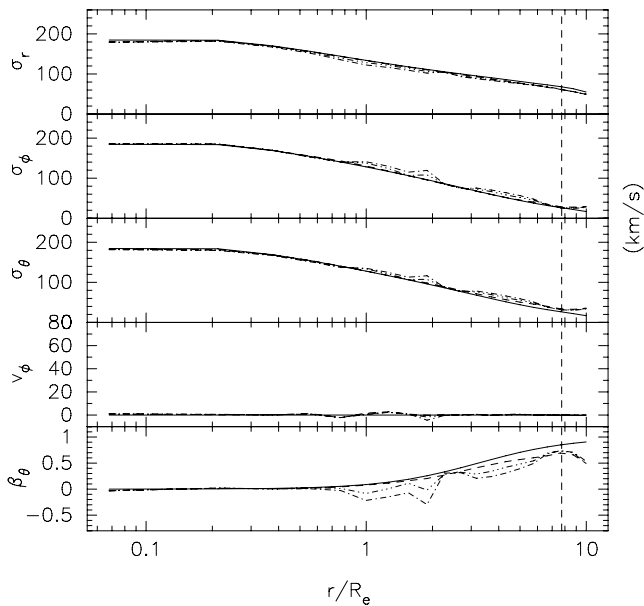
**Figure 8.** Top: deviation rms  $\Delta(\mu)$  between the internal velocity moments of the final mock galaxy particle model and the input model. The upper and lower curves show the rms  $\Delta(\mu)$  obtained, respectively, with the original mock PN velocity dispersion points, and with the errors of these dispersions reduced to  $5 \text{ km s}^{-1}$ . Bottom: the circles show  $\chi^2$  per data point of the model fit to the kinematic and photometric targets as a function of entropy parameter  $\mu$ . The triangles display the merit function  $F$  (cf. equation 6). For both quantities, the curves obtained with the two sets of errors fall on top of each other. The full symbol indicates the optimal value chosen for  $\mu$ .

Fig. 5 shows the target kinematics along the galactic major axis and the corresponding particle model kinematics. Fig. 6 compares the SAURON mock data with the two-dimensional kinematics obtained from the particle model. Fig. 7 shows the PN velocity dispersion data and compares to the model dispersion profiles. All kinematic data are fit very well by the model. In fact, it is evident from Fig. 6 that the model is smoother than the mock data themselves, which is a consequence of entropy-smoothing and time-smoothing.

Fig. 9 shows how well the internal kinematics of the particle model for  $\mu = 2 \times 10^3$  compare with the intrinsic kinematics of the mock galaxy target. The velocity dispersions  $\sigma_r, \sigma_\phi$  and  $\sigma_\theta$ , the streaming rotation  $v_\phi$  and also the anisotropy parameter  $\beta_\theta = 1 - \sigma_\theta^2/\sigma_r^2$  are reproduced well by the model within  $\approx 1R_e$ . At larger radii, the anisotropy of the Osipkov–Merritt DF cannot be entirely recovered even with idealized data (many dispersion points with small error bars), because there is no constraint from the data on the outer particle model (beyond the dashed line in Fig. 9). This is consistent with similar tests in Thomas et al. (2004). With fewer mock PN dispersion data points and larger errors, the particle model obtained from the target data and isotropic initial conditions is less tightly constrained; it becomes even less radially anisotropic despite fitting the actual PN data points well.

### 3.4.1 Mass-to-light ratio

So far all model fits have been made with the mass-to-light ratio fixed to the actual value used for the mock galaxy,  $\Upsilon = 5$ . Now we investigate how accurately we can recover  $\Upsilon$  with the dynamical models, given the spatial extent and quality of the observational data. To this end, we fit particle models to the mock galaxy observations



**Figure 9.** Internal kinematics of the anisotropic target galaxy and its final particle model realizations. From top to bottom:  $\sigma_r$ ,  $\sigma_\phi$ ,  $\sigma_\theta$ ,  $v_\phi$  and anisotropy parameter  $\beta_\theta = 1 - \sigma_\theta^2/\sigma_r^2$ . The kinematic quantities of the input mock galaxy are shown by solid lines, and are compared to those of three different particle models generated for  $\mu = 2 \times 10^3$ : for idealized PN data (many points with small errors, dashed line), for mock data equivalent to the corresponding NGC 3379 data (dot-dashed), and to NGC 3379-like PN data with errors and scatter in the dispersion points reduced to  $5 \text{ km s}^{-1}$  (dash-triple-dot); see Fig. 7.

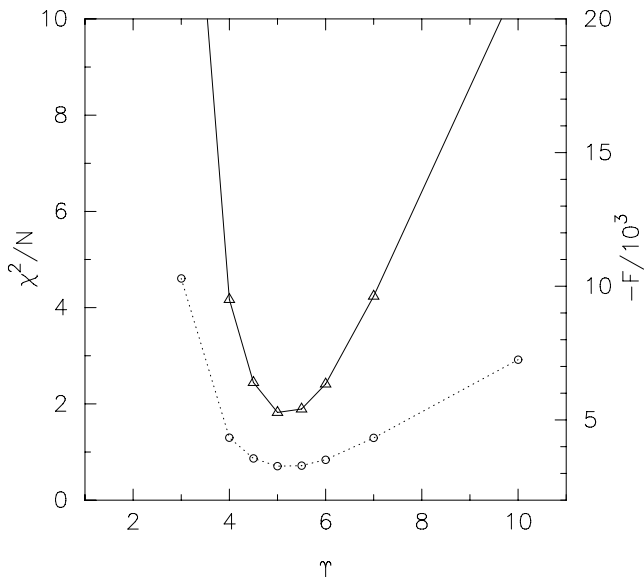


**Figure 10.** Recovering the mass-to-light ratio of the mock galaxy. The quality of the model fit as a function of mass-to-light  $\Upsilon$  is shown in terms of  $\chi^2$  per data point (circles) and merit function  $F$  (triangles). All models are generated from the target pseudo data for  $\mu = 2 \times 10^3$ . The input mass-to-light ratio  $\Upsilon = 5$  is recovered as the minimum in the curve  $\chi^2/N(\Upsilon)$ , where the model fit has  $\chi^2/N \simeq 0.7$ .

for different mass-to-light ratios in the range  $\Upsilon \in [3, 10]$ , keeping the entropy parameter fixed at  $\mu = 2 \times 10^3$ . The results are presented in Fig. 10, which shows how the quality of the model fit varies as a function of  $\Upsilon$ , both in terms of  $\chi^2$  per data point and merit function

$F$ . As expected, the best model is obtained for  $\Upsilon = 5$ ; it has  $\chi^2$  per data point of approximately 0.7.

#### 4 DYNAMICAL MODELS OF NGC 3379

In this section, we construct dynamical models for NGC 3379 to learn about its stellar and DM distribution. We investigate spherical, axisymmetric and some triaxial models, with and without DM haloes, and fit the photometry, SAURON integral field data, slit kinematics and PNe velocity data. Our aim in this paper is not to constrain the detailed halo mass profile of the galaxy, but only to ascertain whether a DM halo is allowed, or required, by the kinematic data. Thus, as in de Lorenzi et al. (2008), we investigate a simple sequence of potentials which include the self-consistent part from the stellar component and a fixed halo potential as in equation (1). The circular speed curves corresponding to these potentials vary at large radii from the near-Keplerian decline expected when the mass in stars dominates, to the nearly flat shapes generated by massive haloes. They are shown in Fig. 11 and their halo potential parameters are given in Table 1.

In the following subsections, we describe spherical models (Section 4.1) and oblate models (Section 4.2), as well as a few triaxial models constructed without imposed axisymmetry constraints (Section 4.3), and then discuss the significance of the fits to the data in a separate subsection (Section 4.4). To begin, with we construct self-consistent particle models for NGC 3379 in which the distribution of stars is spherical. This allows for an easy comparison with previous work (Romanowsky et al. 2003; Douglas et al. 2007).

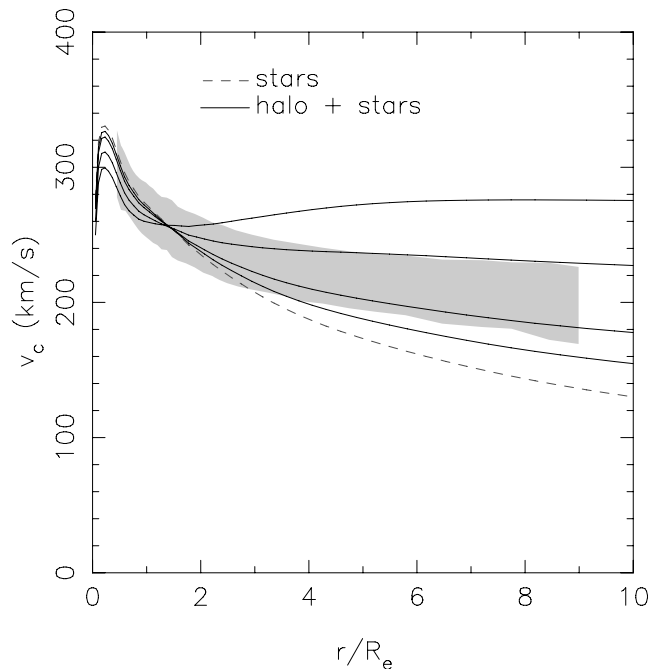


**Figure 11.** Circular velocity curves for the potentials used in the dynamical modelling, including the self-consistent stars-only model A (dashed line) and models including different spherical dark matter haloes in addition to the stellar component (solid lines, from bottom to top: models B, C, D and E). For this figure, the distribution of stars is assumed to be spherical with mass-to-light ratio as given by the final  $\text{NMAGIC}$  model for the data in the respective spherical potential. The shaded area shows the range of circular velocity curves in the merger models discussed by Dekel et al. (2005); see Section 5.

**Table 1.** Table of parameters and fit results for models of NGC 3379 with spherical potentials. Models A–E correspond to the circular rotation curves in Fig. 11. Model D<sup>+</sup> is the same as D but for a higher value of the entropy. Model E\* is the self-flattened oblate model in halo E of Section 4.2.1. For these models columns 1–3 give the model code and the parameters  $r_0$  and  $v_0$  used in equation (1) for the respective dark halo potential. The next six columns list the  $\chi^2$  values per data point, for all observables (column 4) and for the luminosity density and surface brightness constraints, the SAURON kinematic observables, slit kinematic observables and PN observables separately (columns 5–9). Column 10 gives the numerical value of the merit function in equation (6) and column 11 the final (B-band) mass-to-light ratio. The respective number of constraints are  $N = 12997$  for A–E and  $N = 12557$  for E\*, with  $N_{alm} = 640$ ,  $N_{sb} = 200$ ,  $N_{sau} = 11\,214$ ,  $N_{sl} = 1135$ ,  $N_{PN} = 8$ .

Halo	$r_0/R_e$	$v_0/\text{km s}^{-1}$	$\chi^2/N$	$\chi_{alm}^2/N_{alm}$	$\chi_{sb}^2/N_{sb}$	$\chi_{sau}^2/N_{sau}$	$\chi_{sl}^2/N_{sl}$	$\chi_{PN}^2/N_{PN}$	$-F$	$\Upsilon$
A	0	0	0.208	0.137	–	0.176	0.565	0.371	2131.3	8.23
B	3	90	0.215	0.162	–	0.184	0.548	0.323	2231.9	8.03
C	3	130	0.216	0.201	–	0.184	0.539	0.340	2320.1	7.82
D	3	200	0.219	0.271	–	0.186	0.522	0.564	2622.9	7.28
D <sup>+</sup>	3	200	0.362	0.641	–	0.300	0.814	1.002	4409.2	7.57
E	3	260	0.237	0.484	–	0.192	0.535	1.557	3175.2	6.73
E*	3	260	0.241	–	0.084	0.215	0.522	0.504	2649.4	6.52

## 4.1 Spherical models

### 4.1.1 Target data and modelling process

First we must determine the photometric and kinematic observables. Analogous to Section 3.4, we use the spherical harmonics expansion coefficients  $A_{lm}$  of the deprojected luminosity density as target data to constrain the particle models. Specifically, we use  $A_{00}, A_{20}, A_{22}, \dot{c}, A_{66}$ , but set all terms higher than  $A_{00}$  to zero, adopting the same radial grid as in Section 3.4. Errors for the luminosity terms are estimated as in Section 3.4. As kinematic observables, we use the SAURON and slit kinematics, as well as the binned PN velocity dispersion profile (see Sections 2.3 and 3.2). The SAURON data and most slit data are symmetrized, only the slit parallel to their minor axis of Kronawitter et al. (2000) cannot be symmetrized and for this slit the original kinematic data points are used.

We match the particle models to these data in the following three-step process. (i) We begin with the initial particle distribution described in Section 3.3 and evolve it with NMAGIC to a self-consistent model that reproduces the target  $A_{lm}$ . (ii) Starting with this density model, we then construct dynamical models, fitting the full set of photometric and kinematic target observables. If the potential includes a DM halo, we first relax the density model for 1000 steps in the total gravitational potential (cf. Section 3.1), assuming a mass-to-light ratio of 8, to make sure that the model is in approximate equilibrium. After this relaxation phase, we evolve the particle system for  $\sim 10^5$  NMAGIC correction steps while applying the complete set of constraints. During the correction phase, the mass-to-light ratio  $\Upsilon$  is adjusted in parallel, using its own FOC equation as given in de Lorenzi et al. (2008). After each correction step, the potential generated by the particles is updated but the DM potential (if present) is constant in time. In this process, the entropy parameter has value  $\mu = 2 \times 10^3$  (cf. Sections 3.4 and 4.1.3). (iii) In the final step, we keep the global potential constant and evolve the system freely for another 5000 steps, without changing the particle weights (phase-mixing). This completes the modelling process. Thereafter, we generally evolve the model with all potential terms active for a further 10 000 steps to test its stability. For reference, 10 000 correction steps in the self-consistent potential correspond to  $\approx 110$  circular rotation periods at  $R_e$  or 5.8 Gyr.

### 4.1.2 Results

In this way, we obtain spherical dynamical models for NGC 3379, reproducing the density expansion and all kinematic data including

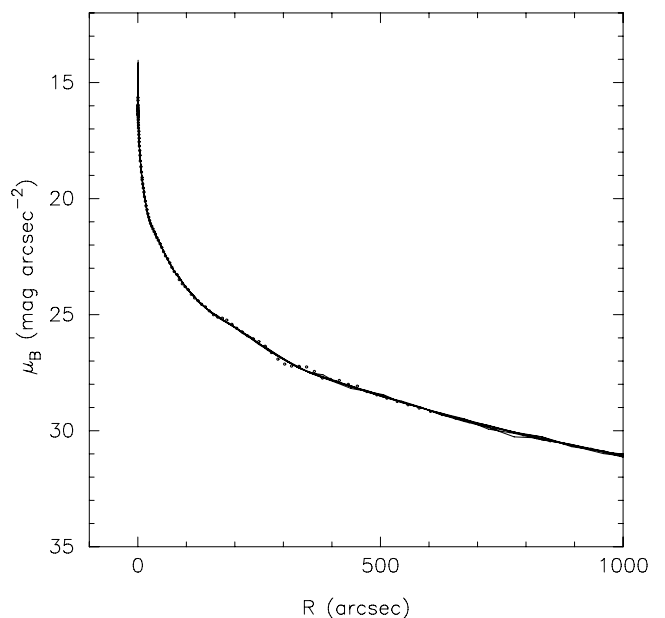


**Figure 12.** Comparison of the surface brightness profiles of the reprojected spherical models with the photometric data (points). The lines are for the spherical models A–E and the self-flattened model E\*. The surface brightness was not directly fitted.

the PN velocity dispersion profile. Model A is the self-consistent model without DM halo, models B–E have haloes of increasing circular velocities, as shown in Fig. 11 and Table 1. The quality of fit for these models can be judged from Table 1, which gives the numerical values of the merit function  $F$  and lists various values of  $\chi^2$  per data point, both those obtained globally for all the data and those found for each of the four data sets separately (density expansion, SAURON, slit and PNe). The  $3\sigma$  outlier point discussed in Section 2.3.2 is not included in the modelling and in the  $\chi_{PN}^2$  in Table 1, but its influence will be discussed below.

Figs 12–15 compare the different data with the models. Fig. 12 shows the SB profiles, Fig. 13 the integral field LOSVD parameter fields, Fig. 14 the kinematics along several slits and Fig. 15 the PN velocity dispersion profiles. The model SB profiles fit the observed profile very well and agree with each other within the thickness of the lines in the plot. The SAURON data are fitted with  $\chi_{sau}^2/N_{sau} \simeq 0.2$  by all our spherical models. Notice that the particle noise in

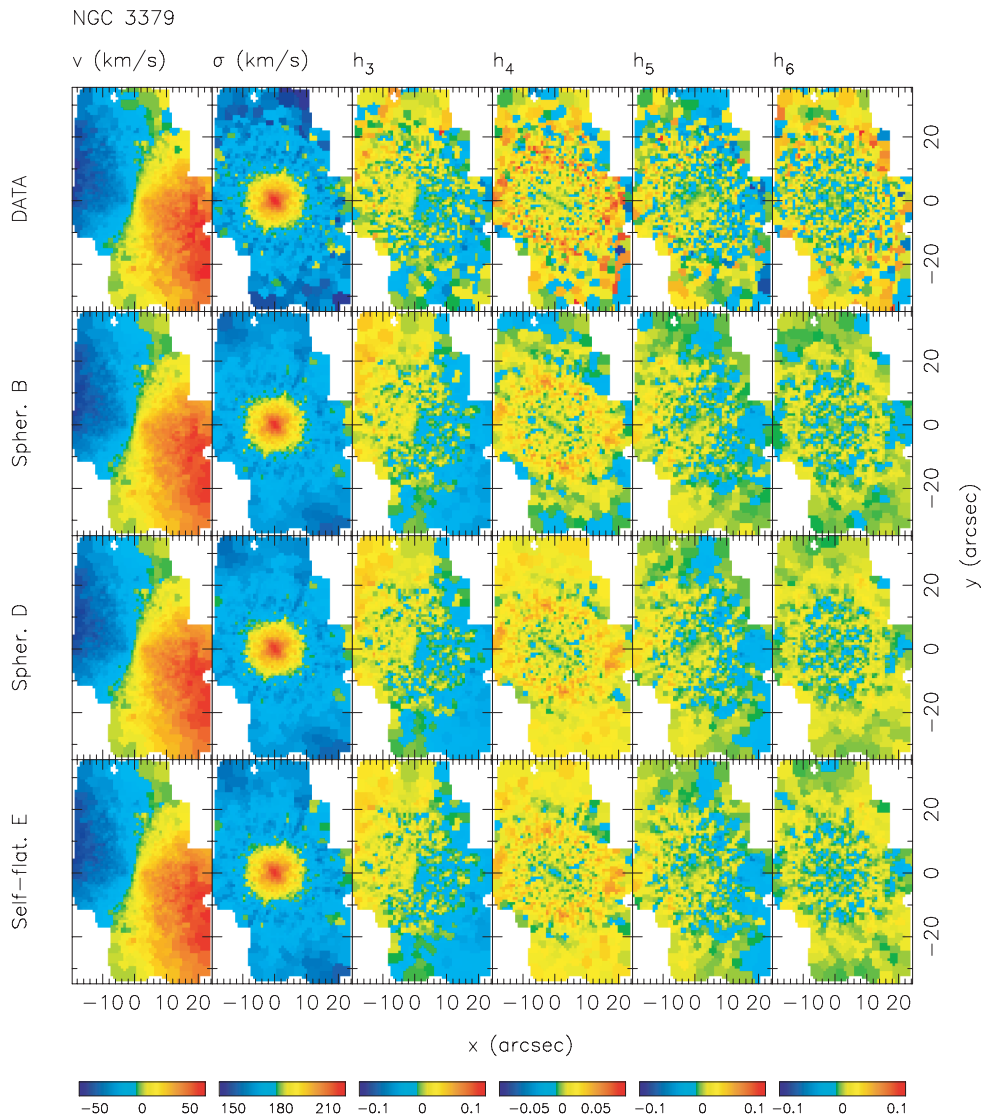


**Figure 13.** Symmetrized SAURON kinematic data for NGC 3379 (top row) compared with similar data extracted for the spherical models B and D and the self-flattened model E\* (lower three rows). Note that the particle noise in the model panels is smaller than the noise in the corresponding data fields for all LOSVD parameters shown. In the panels for  $\sigma$  and  $h_4$ , a slightly colder ring-like structure with larger  $h_4$  hints at some deviations from spherical symmetry.

the models is smaller than the noise in the symmetrized Sauron maps. Also the  $\chi^2_{\text{sl}}/N_{\text{sl}}$  for the combined slit data are less than unity; the plots for models (B, D) in Fig. 14 show a few small systematic deviations but generally the fits are very good. In the central 30 arcsec, the slit data are dominated by the SAURON data. Note that these spherical models are not constrained to be spherically symmetric also in their *kinematic* properties; hence, they can also fit the observed ( $\lesssim 50 \text{ km s}^{-1}$ ) rotation of NGC 3379 with high accuracy. The small  $\chi^2$ -values are caused by the fact that the observational errors are slightly larger than the point-to-point fluctuations (see Fig. 3), and to a greater extent, because with the entropy scheme we cannot smooth the models too much without erasing their anisotropic phase-space structure (cf. Sections 3.4, 4.1.3 and de Lorenzi et al. 2008).

The comparison of the models to the PNS data is shown in Fig. 15. If we use the outermost dispersion point as given in Douglas et al. (2007), models A–D with no or moderately massive haloes provide a good match to the data, but the most massive halo model E fits less

well, being high by  $\simeq 2\sigma$  with respect to the outermost dispersion point and by  $\simeq 1.3\sigma$  with respect to the second outermost point. If we include the object classified as  $3\sigma$  ‘friendless’ outlier (see Section 2.3.2 and Douglas et al. 2007) in the outermost bin, the  $1\sigma$  error range of the outermost PN dispersion point extends to significantly larger velocities (see the red open circle and error bar in Fig. 15). Then, model E also fits the PN dispersion profile, overestimating the outermost velocity dispersion point by less than  $1\sigma$ .

The intrinsic kinematics of these spherical models is shown in Fig. 16. One recognizes the expected signature of the well-known mass-anisotropy degeneracy (Binney & Mamon 1982). In the more massive haloes, the same falling line-of-sight dispersion profile requires larger radial anisotropy. Thus, in the models with halo, the radial anisotropy rises outside  $1-2R_e$ . Particularly, the more massive halo models D and E require strongly radially anisotropic orbit distributions ( $\beta \simeq 0.9$ ) to be consistent with the falling dispersion profile of NGC 3379. Radial anisotropy was suggested as

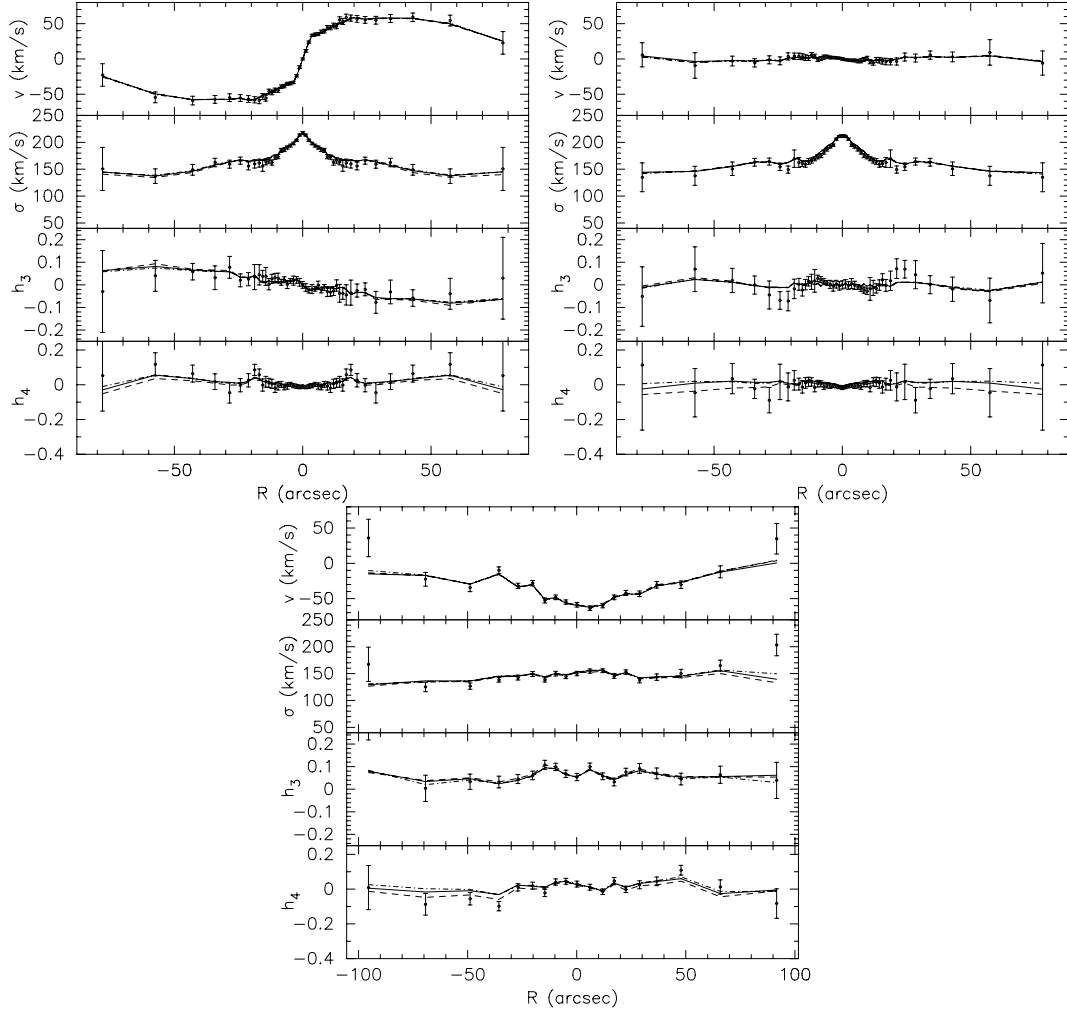


**Figure 14.** Comparison of models B (dashed lines), D (full lines) and E\* (dash-dotted lines) with the symmetrized slit data along the major and minor axes from Statler & Smecker-Hane (1999) (top left and right panel) and the unsymmetrized minor-axis parallel slit from Kronawitter et al. (2000) (bottom panel). The model data points are averages over the same slit cells as the target data (see Fig. 2) and are connected by straight line segments.

one of the possible causes for the measured profile by Dekel et al. (2005), based on a comparison with their merger models. However, the typical anisotropies in their models are more moderate ( $\beta \simeq 0.5$ ).

Despite their strong radial anisotropy, the massive halo models D and E show no sign of an instability when evolved freely after the model fitting and phase mixing. Rather, they evolve very slowly, reaching after 5.8 Gyr of evolution a configuration with slightly triaxial shape in which the initial slow rotation has mostly gone away. A similar evolution is seen for the near-isotropic model A without DM halo, indicating that this evolution may be connected to these equilibria being spherically symmetric only in their mass distribution but, due to the rotation, not in their kinematics. In any case, the PN dispersion profiles do not change during the evolution, i.e. the constraints on the DM halo remain as before.

In conclusion, the results of this section show that both near-isotropic spherical models with low density DM haloes and radially anisotropic spherical models with massive haloes provide excellent fits to the available kinematic data for NGC 3379, including the PN dispersion profile to  $\sim 7R_e$ . A more quantitative discussion is deferred to Section 4.4.

#### 4.1.3 Entropy smoothing

The entropy term in the FOC equation (5) smoothes the particle models by trying to maintain the values of the particle weights near their priors, here chosen as  $1/N$ . Because all models start from an isotropic system with equal weight particles, the entropy smoothing thus biases the final models towards isotropy and slow rotation. To allow the models to develop strong radial anisotropy in their outer parts requires a relatively low value of the entropy parameter (see Section 3.4), which is below that appropriate for an isotropic system. Otherwise, the constraints from the small number of PN dispersion points with their relatively large Poisson error bars would be overwhelmed by the entropy smoothing. We demonstrate this in Fig. 15 and Table 1 with a model D<sup>+</sup> constructed with  $\mu = 2 \times 10^4$ ; this model is indeed degraded in its ability to fit the PNe data, relative to model D which is for the standard  $\mu = 2 \times 10^3$  in the same halo.

Contrary to second derivative regularization, say, entropy smoothing does not distinguish between local and global uniformity of the particle weights; it likes to have *all* particle weights similar to their priors. Thus, if  $\mu$  is chosen so as to allow large

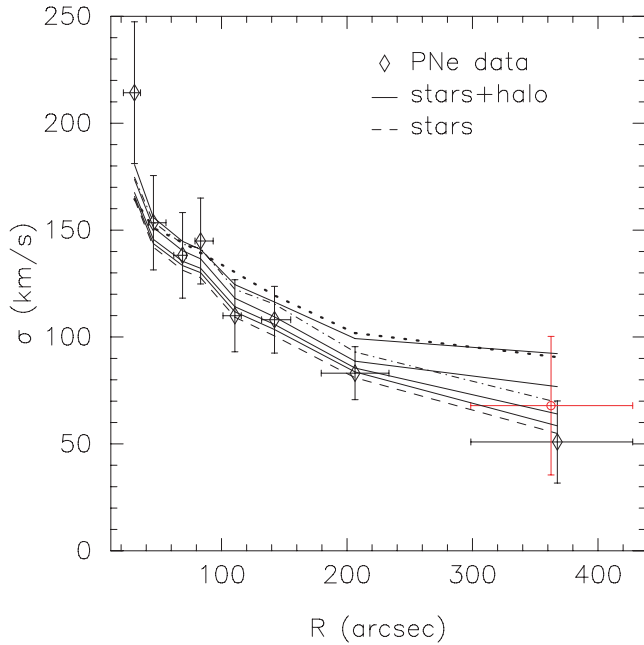


**Figure 15.** Comparison of the PNe velocity dispersion profiles of the spherical models with the PNS data. The PNe velocity dispersion points of Douglas et al. (2007) are shown as black diamonds; when the object classified by them as  $3\sigma$  ‘friendless’ outlier is included, the  $1\sigma$  error range of the outermost PN dispersion point extends to significantly larger velocities (red open circle). The dashed line shows the self-consistent particle model A. The solid lines represent the dynamical models including a DM halo, i.e. from bottom to top models B, C, D and E. The heavy dotted line is for the higher-entropy model  $D^+$ , and the dash-dotted line is for the self-flattened model  $E^*$ .

differences in weight between radial and circular orbits, it also allows similar differences between particles on neighbouring orbits if this is preferred by the data. With  $\mu = 2 \times 10^3$ , the models can therefore fit the data with  $\chi^2/N < 1$  as seen in Table 1. The effect is strongest for the spherical models because these have a larger number of independent orbits than less symmetric systems. However, Fig. 16 shows that the intrinsic velocity moments are smooth functions of radius, and below we will see that also the LOSVDs are smooth functions. The smoothness of the LOSVDs suggests that the good fits of the various models to the PN data are not achieved by large local variations of the particle weights contributing to the PN data points.

## 4.2 Oblate models including dark matter haloes

There is some evidence that NGC 3379 may be non-spherical. Capaccioli et al. (1991) argued that the bulge of NGC 3379 is remarkably similar to the one of NGC 3115, a well-known S0 galaxy. Further, the SAURON kinematic data also, shown in the upper panel of Fig. 13, show signatures of non-sphericity, particularly, a faint cold ring visible in the velocity dispersion and  $h_4$  panels with projected radius  $R \approx 15$  arcsec.<sup>1</sup> Thus, to understand how much dark mass around NGC 3379 is allowed by the kinematic data for this galaxy may require more general models than spherical ones. In this

<sup>1</sup> As can be seen from Fig. 13, the feature can also be reproduced in spherical models.

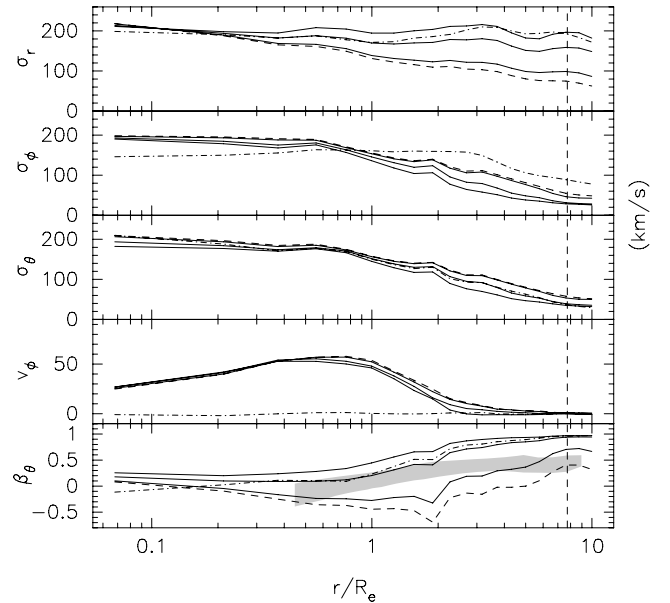


**Figure 16.** Intrinsic kinematics of the final spherical models A (dashed lines) and B,D,E (full lines) and the self-flattened model  $E^*$  (dash-dotted lines). Panels from top to bottom show the radial, azimuthal and vertical velocity dispersion profiles, the mean azimuthal streaming velocity and the meridional anisotropy profile, all computed in an equatorial plane through the model (perpendicular to the rotation axis for the spherical models and perpendicular to the line-of-sight for model  $E^*$ ). The models in the more massive dark matter haloes are more radially anisotropic, as expected. The shaded area in the lower panel corresponds to the range of anisotropy profiles found in the elliptical galaxy remnants in the merger simulations of Dekel et al. (2005).

section, we will present oblate axisymmetric models in the family of spherical halo potentials considered already in the last section.

### 4.2.1 Face-on oblate model in a spherical potential

As a first step, we attempt to construct a model for NGC 3379 in a massive dark halo, in which the distribution of stars is flattened along the line of sight. This model is required to have a small line-of-sight velocity dispersion at large radii, thus will be flattened in accordance with the virial theorem (e.g. Binney & Tremaine 1987). We do not know beforehand what the required shape of this model must be, so we will use the `NMAGIC` method to find it for us. Throughout this experiment the gravitational potential is constrained to remain spherically symmetric, being the sum of the spherical part of the luminous matter potential and the spherical halo potential. For illustration, we embed this model in halo E, and will hence hereafter denote it as model  $E^*$ .

To construct this model, we replace the  $A_{lm}$  constraints (cf. Section 4.1), which earlier imposed a spherical shape on the particle distribution, by the Fourier moments of the SB distribution given in Fig. 1. They are computed from the photometry as in Section 3.2, on a grid in projected radius quasi-logarithmically spaced between  $R_{\min} = 0.01$  arcsec and  $R_{\max} = 1500$  arcsec. The higher-order moments are set to zero, enforcing axisymmetry. We then start from spherical initial conditions and use `NMAGIC` to flatten the particle model through fitting the kinematic observables, particularly the PN velocity dispersion profile. As kinematic constraints, we use the SAURON, slit and PNe velocity dispersion data. The entropy parameter is kept at the same value as for the spherical models,

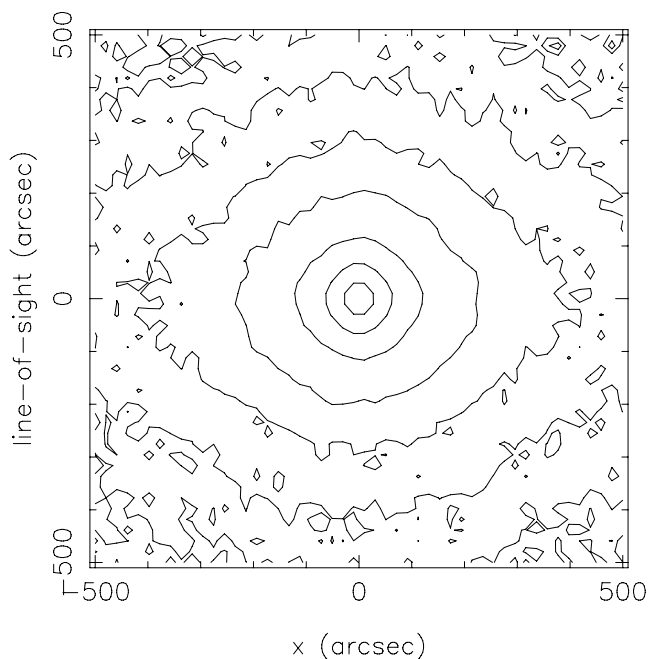


**Figure 17.** Surface brightness contours of the kinematically deprojected oblate model E\*, when viewed perpendicular to the line-of-sight, i.e. edge-on. The model’s outer parts have been preferentially flattened to match the falling PN velocity dispersion profile.

$\mu = 2 \times 10^3$ . During this ‘kinematic deprojection’, the spherically averaged potential generated by the particles is updated after regular time intervals, but the non-spherical terms are ignored. The DM potential is given by equation (1) and remains constant in time. After the correction phase, the model is again allowed to freely evolve for some time.

Figs 12–15 show how the final ‘self-flattened’ particle model E\* compares to the various data. The model fits the data as well as the best-fitting spherical models. As anticipated, the model makes the PN dispersion profile compatible with a massive dark halo potential by flattening the outer distribution of stars and decreasing the model  $\sigma$  along the line-of-sight. Fig. 16 shows that the ratio of the line-of-sight velocity dispersion measured in the equatorial plane ( $\sigma_\theta$ ) to the  $\phi$ -dispersion in this plane decreases with radius. At  $\sim 2R_e$ , it is  $\simeq 0.8$  and falls off to  $\simeq 0.5$  at  $\sim 7R_e$ . However, the radial velocity dispersion also dominates in this model. The model’s flattening is illustrated in Fig. 17, which shows the SB distribution in an edge-on projection perpendicular to the line-of-sight. The axis ratio is  $q \simeq 0.7$ , but to match the decreasing line-of-sight velocity dispersion profile, the flattening increases at large radii.

While this model illustrates the power of the *NMAGIC* method, and provides an excellent fit to the photometric and kinematic data in a massive dark DM halo, it is not a realistic model for NGC 3379. For it is only in a spherical potential as assumed for model E\* that a face-on distribution of stars can show rotation. More realistic axisymmetric models must therefore be inclined to allow for the rotation seen in the SAURON and slit data.

#### 4.2.2 Self-consistent oblate models

Therefore, we now consider oblate models for NGC 3379 with inclinations  $i = 90^\circ$ ,  $i = 50^\circ$  and  $i = 40^\circ$ , in which the axisymmetric

gravitational potential of the stellar component is computed self-consistently from the particles, but the DM halo is treated as before. Also the procedure for constructing the models is similar to that in Section 4.1. We compute for each inclination  $L_k$  and the higher order moments  $A_{20}, A_{22}, \dots, A_{66}$ , but set the  $m \neq 0$  terms of the expansion to zero to force the models to remain axisymmetric. Errors for the  $A_{lm}$  coefficients are estimated as in Section 3.4. We thus obtain three different sets of luminosity density observables  $A_{lm}$  with corresponding errors, one for each of the three inclinations. In addition to the  $A_{lm}$ , we also use the SB itself as a constraint, through the Fourier moment observables on the grid of projected radii  $R_k$  as in the previous Section 4.2.1. Errors for these Fourier moments are computed similarly as the  $A_{lm}$  errors. The kinematic constraints are identical to those used for the spherical models.

For the combined set of observables, we construct particle models in a similar three-step process as for the spherical models. The quality of the fit for the different halo models and inclinations are summarized in Table 2 and will be discussed further in Section 4.4. In addition to the models shown in Table 2, we have also constructed a similar suite of models for the unsymmetrized SAURON and slit data. These models were of similar quality as the models for the symmetrized data, i.e. when subtracting the systematic error floors determined in Section 2.3.1 [ $\chi^2_{\text{sau}}/N_{\text{sau}}(\text{sys}) = 1.0$  and  $\chi^2_{\text{sl}}/N_{\text{sl}}(\text{sys}) = 1.0$ ] from the  $\chi^2$  values of the models for the unsymmetrized data, the model  $\chi^2$  values became very similar to those reported in Table 2.

Figs 18–20 compare some of the final axisymmetric particle models to the SAURON, slit and PNe data. Both edge-on and inclined models again are very good matches to the SAURON and slit data, with or without DM halo. The PN velocity dispersion profile is fitted well by the models with the lower mass halo models B, C; halo D slightly overestimates the outer PN velocity dispersion point given by Douglas et al. (2007) but is within  $1\sigma$  of the outer point when the ‘friendless’ outlier is included. Model E90 is inconsistent with the outer dispersion point of Douglas et al. (2007) (cf. Table 2), but is only marginally inconsistent with the data when the outlier is included. Based on this together with the likelihood results reported below, halo D is the most massive halo consistent with the PN data. Fig. 21 shows that for this model the dark halo contributes about 60 per cent of the total mass within the radius of the last PN data point at  $\sim 7R_e \sim 15$  kpc.

Fig. 22 shows the intrinsic velocity dispersions, streaming velocity and anisotropy for some of the models. Because of the small projected ellipticity of NGC 3379 and the assumed spherical DM halo, the edge-on models are very similar to the spherical models in the respective halo potentials and the higher circular velocity haloes require large radial anisotropy to match the PN data. The inclined flattened models have similarly small  $\sigma_z = \sigma_\theta$  in the model equatorial plane, but somewhat larger  $\sigma_\phi$ , as expected. Also in the axisymmetric models it is the radially increasing, strong radial anisotropy which causes the rapidly decreasing PN velocity dispersion profile in the massive dark halo potentials.

Finally, we comment briefly on the stability of these models. All models in haloes A–C show no signs of any change after 5.8 Gyr of evolution following the phase mixing after the *NMAGIC* fit. The D models are almost unchanged, despite the strong radial anisotropy, developing after 5.8 Gyr a percent-level triaxiality just outside the error bars of the  $A_{22}$  constraints. The models in halo E show a similar slow evolution during which they in addition develop significant positive  $h_4$  across the entire image. As in the spherical models, the PN dispersion profiles remain unchanged during this evolution.

**Table 2.** Table of parameters and  $\chi^2$ -fit results for oblate and triaxial models of NGC 3379. Columns 1–3 give the model code and the parameters  $r_0, v_0$  used in equation (1) for the respective dark halo potential; all halo potentials are spherical ( $q_\phi = 1.0$ ). The fourth column gives the inclination  $i$  (for the triaxial models this is the angle between the line-of-sight and the short axis), and the next six columns list the  $\chi^2$  values per data point, for all observables (column 5), and for the density constraints, surface brightness constraints, SAURON kinematic observables, slit kinematic observables and PN observables separately (columns 6–10). Column 11 gives the numerical value of the merit function in equation (6), and column 12 the final (*B*-band) mass-to-light ratio. The respective number of constraints are  $N = 13237, N_{alm} = 680, N_{sb} = 200, N_{sau} = 11214, N_{sl} = 1135, N_{PN} = 8$ .

Halo	$r_0/R_e$	$v_0/\text{km s}^{-1}$	$i$	$\chi^2/N$	$\chi^2_{alm}/N_{alm}$	$\chi^2_{sb}/N_{sb}$	$\chi^2_{sau}/N_{sau}$	$\chi^2_{sl}/N_{sl}$	$\chi^2_{PN}/N_{PN}$	$-F$	$\Upsilon$
A90	0	0	90	0.619	0.173	0.331	0.624	0.866	0.369	4899.995	8.09
A50	0	0	50	0.773	0.291	0.437	0.781	1.031	0.426	6129.759	8.12
A40	0	0	40	0.789	0.507	0.587	0.780	1.079	0.515	6634.361	8.22
B90	3	90	90	0.631	0.243	0.40	0.635	0.852	0.344	5051.231	7.923
B50	3	90	50	0.777	0.352	0.523	0.782	1.008	0.371	6196.835	7.97
B40	3	90	40	0.782	0.570	0.670	0.770	1.047	0.438	6562.924	8.10
C90	3	130	90	0.651	0.296	0.457	0.655	0.851	0.401	5291.926	7.72
C50	3	130	50	0.741	0.429	0.611	0.742	0.933	0.396	6030.503	7.82
C40	3	130	40	0.766	0.661	0.591	0.753	0.990	0.414	6478.453	7.98
D90	3	200	90	0.611	0.367	0.462	0.603	0.847	0.887	5343.843	7.26
D50	3	200	50	0.761	0.394	0.663	0.763	0.961	0.815	6394.686	7.50
D40	3	200	40	0.745	0.618	0.639	0.738	0.906	0.654	6466.793	7.693
E90	3	260	90	0.684	0.577	0.751	0.652	1.037	2.602	6325.564	6.86
E50	3	260	50	0.765	0.530	0.854	0.749	1.026	2.401	6782.397	7.20
E40	3	260	40	0.756	0.819	0.739	0.899	0.737	1.662	6806.086	7.42
AR	3	0	47	0.746	–	0.754	0.720	1.005	0.597	6264.9	8.10
BR	3	90	51	0.742	–	0.740	0.718	0.982	0.480	6125.2	7.98
CR	3	130	50	0.737	–	0.480	0.721	0.941	0.427	5976.0	7.80
DR	3	200	46	0.722	–	0.574	0.708	0.881	0.922	6034.2	7.55
ER	3	260	47	0.762	–	1.143	0.733	0.961	3.159	6562.9	7.28

### 4.3 Triaxial models

We have constructed a small number of models for which the stellar density was not constrained to remain axisymmetric, in order to see whether the larger freedom in the orbit structure of non-axisymmetric potentials would allow the models to fit the PN kinematics also in the most massive halo E. However, these models do not have isophote twists: we have kept the constant value  $PA = 70$  deg for the position angle in the photometry, neglecting the observed small variations  $\Delta PA = \pm 3$  deg. These models are generated making use of the full power of NMAGIC: Only the SB and kinematic data are used as constraints, in a similar way as for model E\*, leaving all density  $A_{lm}$  terms and corresponding potential terms free to change during the evolution. This allows these models to freely change their orientation.

As initial conditions, we have constructed particle models in each of the haloes A–E by (i) generating a flattened system analogously to model E\* (see Section 4.2.1), (ii) computing the gravitational potential of the resulting particle distribution and (iii) finally relaxing the particle distribution in the combined potential of the particles and the respective DM halo. The initial models were then evolved with the constraints from the SB and projected kinematics until convergence was reached, while updating the potential of the particle system. Because of the observed line-of-sight streaming velocities, these systems rotate out of the sky plane while NMAGIC simultaneously keeps adjusting the orbit structure to match the observables.

We describe in some more detail the final model DR obtained in halo D. This model converges to an almost axisymmetric model with inclination  $i \simeq 46$  deg, and is then completely stable over 5.8 Gyr of evolution. We have computed iteratively the mean intermediate and minor axis lengths inside ellipsoidal radius  $s = [x^2 + (y/b)^2 + (z/c)^2]^{1/2}$ , following Dubinski & Carlberg (1991). We obtain axis ratios  $b = 0.984$  and  $c = 0.74$  for

$s = 50$  arcsec  $\simeq 2.375$  kpc, and  $b = 0.990$  and  $c = 0.74$  for  $s = 200$  arcsec  $\simeq 9.5$  kpc. Note that the error in these axis ratios is about 0.002, due to the large number of particles used in the diagonalization of the tensor. This weakly triaxial model matches all the kinematic data, SAURON, slit and PNe, very similar to models D40 and D50, and is listed in Table 2 as model DR. Its projected kinematics are shown in Figs 18–20, and the enclosed DM fraction is about 60 per cent of the total mass within the radius of the last PN data point at  $\sim 7R_e \sim 15$  kpc (Fig. 21).

Table 2 shows the  $\chi^2$  results for the entire sequence of models AR–ER, and Fig. 20 compares these models to the PN data. The inclination angles given in Table 2 for the triaxial models are the final angles between principal plane and sky plane (intrinsic short axis and line-of-sight). Within this sequence, the best total  $\chi^2$  are obtained for models CR and DR; these  $\chi^2$  values are similar to those of the axisymmetric models (they are not directly comparable because of the different effective number of degrees of freedom). On account of  $\chi^2_{PN}$ , the best models are BR and CR (these values are computed from the velocity dispersions without the outlier PN). The projected velocity fields of model CR are also shown in Fig. 18.

The model ER in halo E again clearly does not fit the PN data. None of our other attempts to obtain a valid model E has been successful. These included triaxial models starting from different initial conditions (a spherical model, a model flattened along the line-of-sight or the inclined model D40), as well as one inspired by some old work on merger remnants (Gerhard 1983a,b), following which we tried to construct an oblate triaxial model whose inner oblate parts are seen edge-on by the observer, while its triaxial outer regions are observed along the short axis.

We believe the main reason for the failure in halo E is the observed rotation of NGC 3379, of which either the sense (along the projected major axis) or the amplitude do not allow the low-inclination configurations required by the low values of velocity

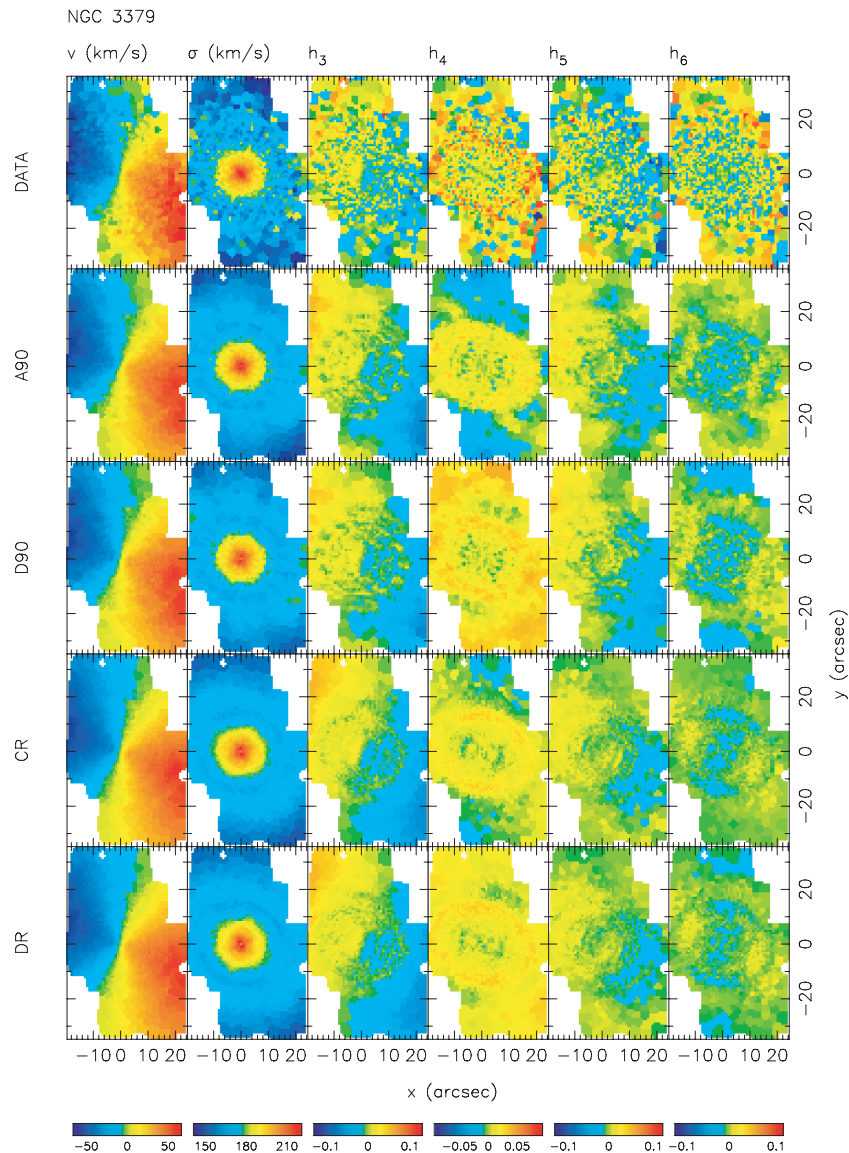


**Figure 18.** Comparison of axisymmetric and weakly triaxial models with SAURON kinematic data for NGC 3379 (top panel). Following panels are for models A90, D90, CR and DR. Model A90 has all the mass in the stars, while the later models include massive haloes; see Table 2.

dispersion at large radii. Consider a triaxial model viewed approximately along the short axis, which could easily accommodate the outer falling dispersion profile by a corresponding change of shape with radius as in model E\*. Such a model is not consistent with the observed rotation, because in this case the rotation visible to the observer would be around the model’s long axis, i.e. it would be observed along the minor axis on the sky, whereas the actual observed rotation is along the major axis on the sky. On the other hand, a triaxial model with minor axis in the sky plane must correspond to a very round model unless it is near-prolate and viewed end-on. Then, the box orbits are also viewed near end-on, making it difficult to arrange a falling outer dispersion profile. Thus, valid triaxial models are likely to either be radially anisotropic and to have similar viewing geometry as model DR or be more edge-on and quite round, so the dominant effect on the inferred potential is the radial anisotropy. While in principle other sequences of triaxial models, possibly including triaxial dark halo potentials, might allow larger dark halo masses in NGC 3379 than corresponding to halo

D, in our view the failure of model ER makes this unlikely. Further study of this issue is beyond the scope of this paper.

#### 4.4 Likelihoods and quality of the fits to the data

We now turn to discussing the question which models are acceptable fits to the data and which models can be ruled out. To do this, it is customary to determine  $\Delta\chi^2$  values relative to the best-fitting models, and determine the confidence boundaries according to the number of parameters to be determined. In our case, we essentially determine only one parameter, the halo circular velocity at  $\sim 7R_e$  or  $v_0$ , so the relevant  $\Delta\chi^2 = 1$  (the mass-to-light ratio of the models is optimized together with the weights). However, all our models match the Sauron and slit kinematic data to within  $1\sigma$  per data point, i.e. formally better than the underlying ‘true’ model (cf. the discussion in Sections 3.4, 4.1.3 and de Lorenzi et al. 2008). Clearly, we cannot apply a  $\Delta\chi^2 = 1$  for small variations within  $1\sigma$  relative to, say, the Sauron data points. Even if the best model fitted with

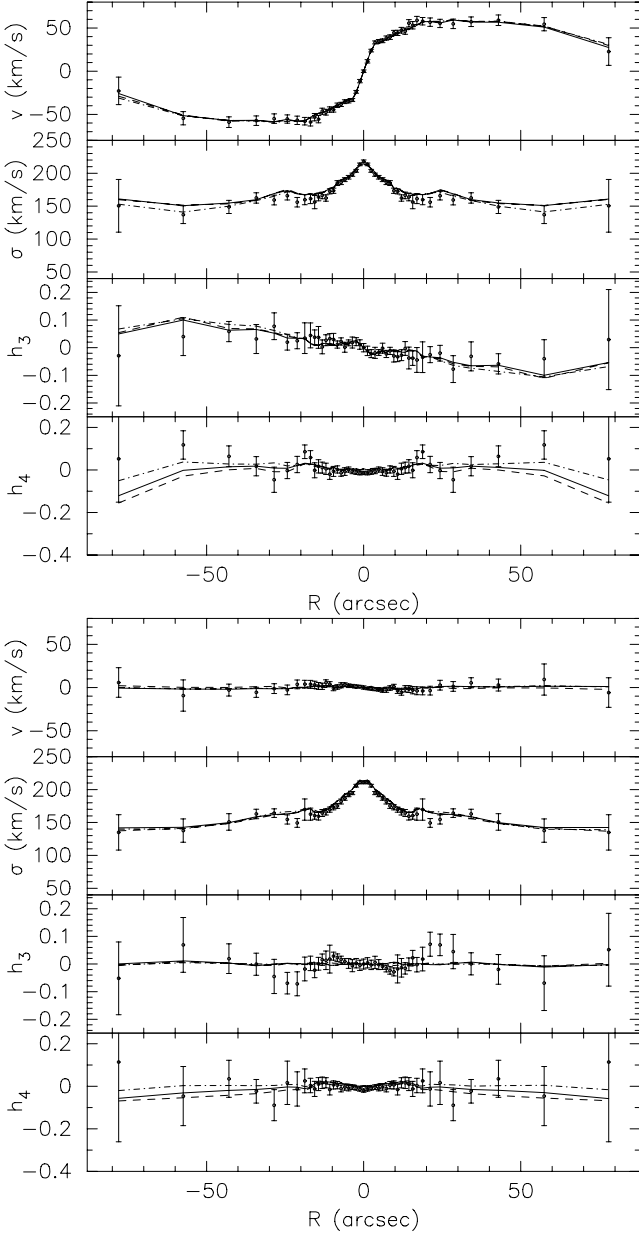


**Figure 19.** Comparison of the axisymmetric models A90 (dashed lines), D90 (full lines) and the weakly triaxial model DR (dash-dotted lines) with the symmetrized slit data from Statler & Smecker-Hane (1999) along the major (top) and minor axes (bottom panel). The model data points are averages over the same slit cells as the target data (see Fig. 2) and are connected by straight line segments.

exactly  $\chi^2_{\text{sau}} \approx 10^4$ , this would make little sense: for  $N_{\text{sau}} = 10^4$ ,  $\Delta\chi^2 = 1$  corresponds to an average change per data point of  $\approx 10^{-4}\sigma$ , which would be easily swamped by systematic effects. Only if the  $\Delta\chi^2 = 1$  arises because of significant mismatch of a few crucial data points would this seem reasonable. The crucial data points for the issue addressed in this paper, the DM halo in NGC 3379, are the PN velocities or the binned PN dispersions. Thus, we focus our discussion on the merit of the models relative to these data.

Fig. 23 shows the  $\chi^2_{\text{PN}}$  and  $\Delta\chi^2$  values for both the spherical and the axisymmetric models from Tables 1 and 2. For the PN dispersion points, we have 7 degrees of freedom (8 data points minus

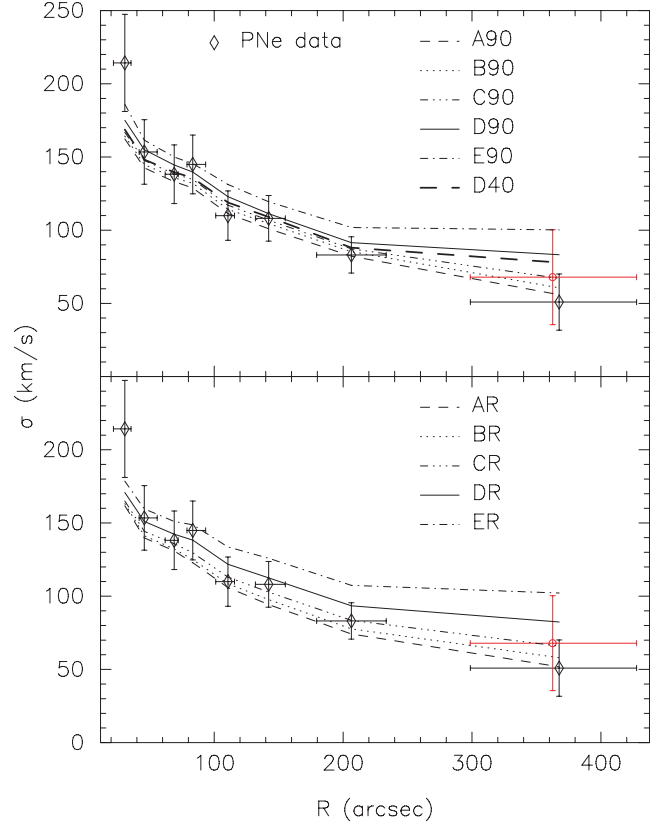


**Figure 20.** Comparison of the radial velocity dispersion profile from the PNS data with the oblate and weakly triaxial particle models. Top panel: axisymmetric models. The dashed line shows the stellar-mass only model A90. The other lines show models B90, C90, D90, D40 and the upper dash-dotted line shows model E90. Bottom panel: triaxial models AR–ER with similar line-styles as in the top panel.

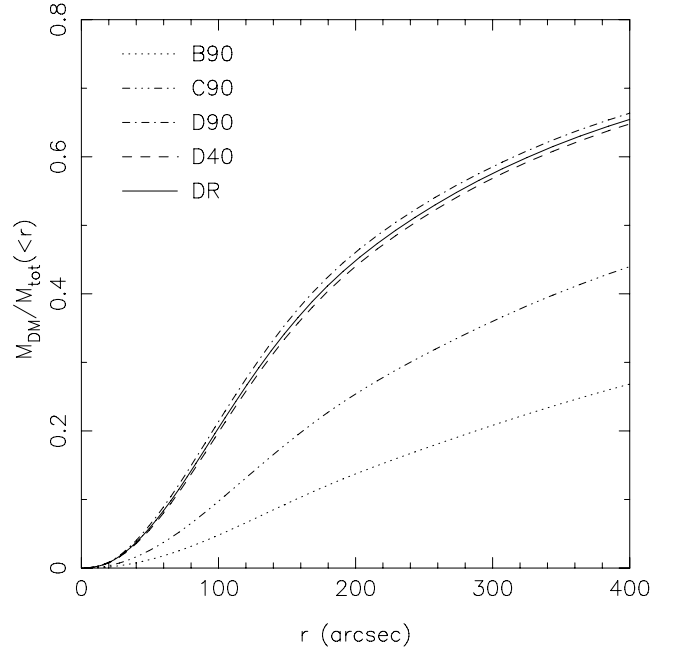


**Figure 21.** Enclosed DM fraction as function of radius for the final particle models B90, C90, D90, D40 and DR.

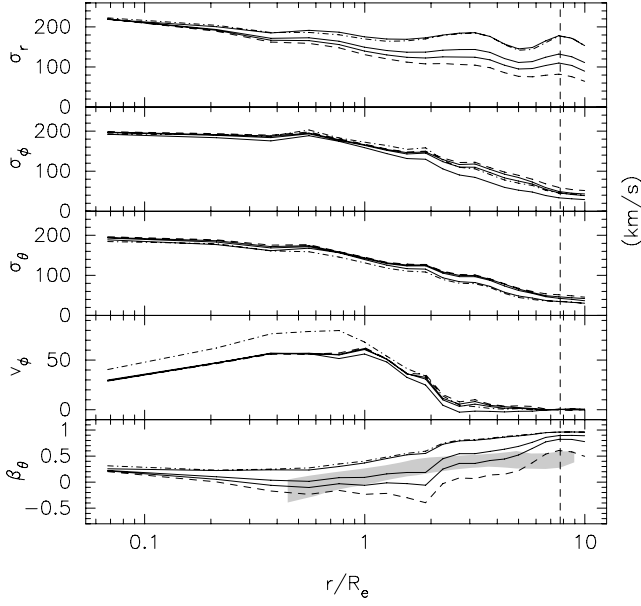


**Figure 22.** Intrinsic kinematics of the final models A90, B90 (dashed), C90, D90 (full) and D50 (dash-dotted lines). Panels from top to bottom show the radial, azimuthal and  $\theta$  velocity dispersion profiles, the mean azimuthal streaming velocity and the meridional anisotropy profile  $\beta_\theta = 1 - \sigma_\theta^2/\sigma_r^2$ . The models in the most massive haloes are strongly radially anisotropic, as expected.

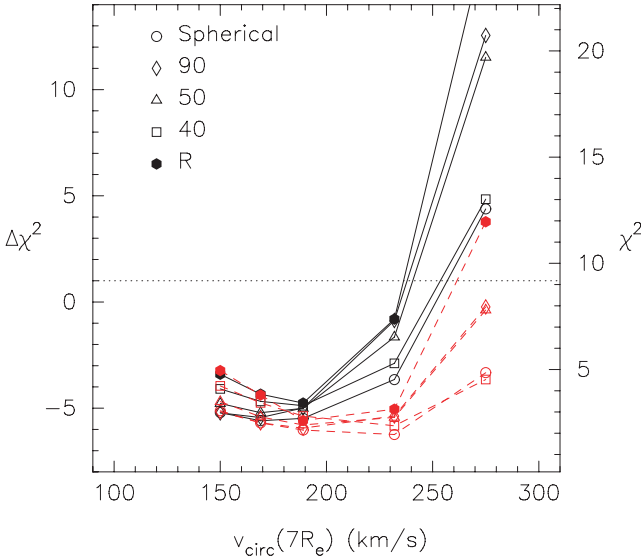


**Figure 23.**  $\chi^2$  and  $\Delta\chi^2$  values of the various spherical, axisymmetric and triaxial models for NGC 3379 with respect to the PN velocity dispersion data. The full black lines (red dashed lines) connect the  $\chi^2$ -values obtained without (including) the  $3\sigma$  ‘friendless’ outlier of Douglas et al. (2007).  $\Delta\chi^2$  is computed relative to the expected value of  $\chi^2 = 8.18$  for 7 degrees of freedom.

1 fitted parameter), so expect  $\chi^2 = 8.18$  (68.3 per cent probability) for a typical good model. Thus, we consider any model that fits the PN velocity dispersions to better than  $\chi^2 = 8.18$  as valid as the underlying ‘true’ model and compute  $\Delta\chi^2$  relative to  $\chi_{\text{PN}}^2 = 8.18$ . The curves in Fig. 23 are plotted for the two cases with and without the ‘friendless’ outlier of Douglas et al. (2007) contributing to the outermost dispersion point. The models with haloes A–D are

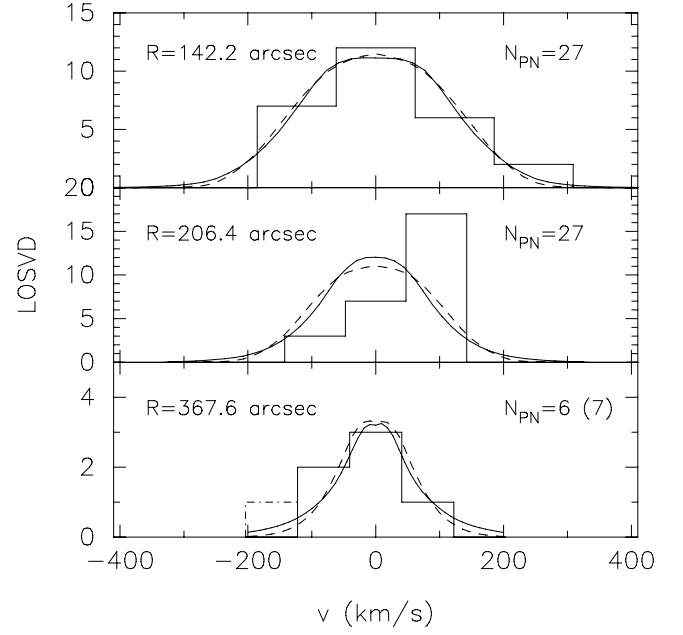


**Figure 24.** Comparison of the PNe LOSVDs in the circular annuli corresponding to the outermost three bins in the velocity dispersion profile, with the LOSVDs of the nearly isotropic, low-density halo model B (dashed lines) and the radially anisotropic massive halo model D (solid lines) in the same circular annuli. The ordinate is in units of PN number and the model LOSVDs have been normalized to the same integral over the velocity range shown. In the middle panel for the second annulus, the mean velocity of the PNe is non-zero at the  $\approx 3\sigma$  level; both models are inconsistent with this velocity distribution. The velocity distributions in the other two panels are fully consistent with both models. In the lower panel for the outermost shell, the PN histogram is shown with (dash-dotted) and without (solid line histogram) the  $3\sigma$  ‘friendless’ outlier (see Section 2.3.2 and Douglas et al. 2007).

allowed in both cases, while models for halo E are consistent with the data only when the outlier is included.

So far we have compared the models only to the PN velocity dispersion profile, rather than to the LOSVDs or unbinned velocity data. Fig. 24 shows the LOSVD histograms for the PNe in the outermost three circular annuli used for computing the PN velocity dispersion profile, superposed on the LOSVDs of models B and D in the same radial shells. In the plot for the outermost bin, the PN histogram and model LOSVD are shown with and without the  $3\sigma$  ‘friendless’ outlier according to Douglas et al. (2007). Both the near-isotropic low-density halo model B and the radially anisotropic massive halo model D are consistent with the PN velocity distributions in the first and third annuli, and both appear inconsistent with the apparent non-zero mean motion of the observed PNe in the second annulus.

Table 3 shows the posterior likelihoods of the spherical models for the observed PN velocity data set, evaluated from the model LOSVDs in the eight radial shells used in the fits. Also listed are the likelihoods resulting from direct likelihood fits of the spherical and triaxial models to the PN data, using the method described in de Lorenzi et al. (2008). Fig. 25 shows a plot of these likelihoods as a function of the models’ circular velocity at  $7R_e$ , the radius of the outermost PN dispersion point. Despite the small number of potentials investigated and the issue of whether the  $3\sigma$  ‘friendless’ outlier should be included, the overall shape of the likelihood

**Table 3.** Likelihood values for the PN data in the spherical and triaxial models. Column 1: model code. Columns 2 and 3: log likelihood  $\ln \mathcal{L}$  and difference  $2\Delta \ln \mathcal{L}$  relative to the best model C, for the PN sample not including the  $3\sigma$  ‘friendless’ outlier in the outermost shell, according to Douglas et al. (2007). Columns 4 and 5: same, but for the PN sample including this outlier. The top third of the table refers to posterior likelihoods of spherical models fitted to the PN velocity dispersion profile, the middle section gives likelihoods for similar models in which the PNe were fitted with the likelihood method of de Lorenzi et al. (2008), and the bottom third gives the likelihoods for the triaxial models obtained with the same likelihood method.

Model	Without outlier		With outlier	
	$\ln \mathcal{L}$	$2\Delta \ln \mathcal{L}$	$\ln \mathcal{L}$	$2\Delta \ln \mathcal{L}$
A	-605.14	2.50	-611.18	4.58
B	-604.21	0.64	-609.67	1.56
C	-603.89	0.00	-608.89	0.00
D	-604.74	1.70	-609.23	0.68
E	-607.16	6.54	-611.38	4.98
A	-608.50	4.23	-613.53	5.01
B	-607.01	1.25	-611.82	1.60
C	-606.38	0.00	-611.02	0.00
D	-606.68	0.60	-611.14	0.23
E	-608.81	4.85	-613.04	4.02
AR	-608.08	5.54	-613.69	7.46
BR	-605.99	1.37	-611.09	2.25
CR	-605.31	0.00	-609.96	0.00
DR	-605.72	0.83	-610.02	0.11
ER	-608.65	6.69	-612.58	5.24

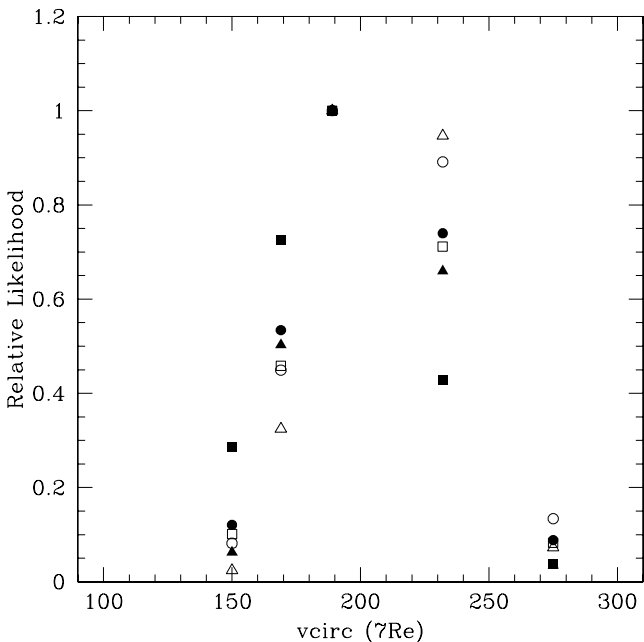


**Figure 25.** Relative likelihoods from the data in Table 3 as a function of the model circular velocity at  $7R_e$ . Squares show posterior likelihoods of spherical models A–E fitted to the binned dispersion profile, circles show likelihood values based on direct likelihood fits to the PN velocities. Triangles show direct likelihood fits of the triaxial models AR–ER to the PN velocities. Filled symbols show likelihoods for the PN sample without the  $3\sigma$  ‘friendless’ outlier in the outermost shell, according to Douglas et al. (2007), open symbols for the sample including this outlier.

function  $\mathcal{L}$  is not too far from the theoretically expected the Gaussian. Thus, we can determine a confidence interval from the condition  $\Delta \log \mathcal{L} > 0.5$ , resulting in approximately  $165 \text{ km s}^{-1} \lesssim v_{\text{circ}}(7R_e) \lesssim 250 \text{ km s}^{-1}$  at  $1\sigma$ . This would exclude both model A without DM and the most massive halo model E. However, we do not believe this is a very strong result, given the influence of a single outlier on the relative likelihood values in Table 3, and the asymmetries in some of the LOSVDs (see Fig. 24). Note also that all models are consistent with the data at the  $2\sigma$  level, for which  $v_{\text{circ}}(7R_e) \lesssim 280 \text{ km s}^{-1}$ .

## 5 SUMMARY AND CONCLUSIONS

In this paper, we have carried out a dynamical study of the elliptical galaxy NGC 3379. This intermediate luminosity E1 galaxy has a rapidly declining velocity dispersion profile, which has been taken as evidence by Romanowsky et al. (2003) and Douglas et al. (2007) that this galaxy may lack the kind of DM halo that the current  $\Lambda$  cold dark matter ( $\Lambda$ CDM) cosmology requires.

To explore this issue further, we have combined photometry, long slit spectroscopic data, SAURON absorption line kinematics and PN velocity dispersion data, to fit dynamical models in a sequence of potentials whose circular velocity curves at large radii vary between a near-Keplerian decline and the nearly flat shapes generated by massive haloes. The combined kinematic data set runs from the centre of NGC 3379 to about 7 effective radii.

For constructing the dynamical models, we have used the flexible  $\chi^2$ M2M particle code NMAGIC developed by de Lorenzi et al. (2007, 2008). The NMAGIC models described in this paper consist of  $7.5 \times 10^5$  particles, and for the first time are constructed for such a comprehensive data set, including integral field kinematic data.

We find that a variety of dynamical models of different shapes, and both with and without DM, produce viable fits to all the data.

For assumed spherical symmetry, we find that the data are consistent both with near-isotropic systems, which are dominated by the stellar mass out to the last kinematic data points, and with models in massive haloes whose outer parts are strongly radially anisotropic [ $\beta(7R_e) \gtrsim 0.8$ ]. In these latter models, the stellar mass distribution dominates in the centre and the DM fraction is  $\sim 60$  per cent of the total at  $7R_e$ .

We have then constructed self-consistent axisymmetric models of inclinations  $i = 90^\circ$ ,  $i = 50^\circ$  and  $i = 40^\circ$  in the same sequence of haloes potentials.  $i = 40^\circ$  is near the limit allowed by the observed photometry and rotation. These models essentially confirm the spherical results. The edge-on models are very similar to the spherical models, becoming highly anisotropic in the more massive haloes. The inclined models in addition become more flattened at large radii, which helps in decreasing the outer velocity dispersion profile.

Finally, we have constructed a sequence of (weakly) triaxial models by free evolution from axisymmetric models flattened along the line-of-sight. These models end at  $i \simeq 47$  deg inclination, are almost axisymmetric, and for the same range of halo masses match all kinematic data very well. All these models are stable over gigayears.

In the spherical and triaxial potentials, we have also used the likelihood scheme of de Lorenzi et al. (2008) to fit the models directly to the PN velocities. From the likelihood values obtained in these fits, as well as the posterior likelihoods of the models fit to the dispersion profiles, we estimate confidence limits on the halo circular velocity at  $7R_e$ , resulting in approximately  $165 \text{ km s}^{-1} \lesssim v_{\text{circ}}(7R_e) \lesssim 250 \text{ km s}^{-1}$  at  $1\sigma$ . This would exclude both the model

without DM and the most massive halo model E in our sequence which has  $v_{\text{circ}}(7R_e) \simeq 275 \text{ km s}^{-1}$ .

To illustrate the power of *NMAGIC*, we have used it to find the shape of a model flattened along the line-of-sight in a spherical potential including this most massive halo E, which fits all the kinematic data with high accuracy. However, all attempts to find more realistic models with this massive halo have failed, suggesting that we may have found the upper limit of the range of consistent mass distributions. This is mostly driven by the observed rotation, which does not allow approximately face-on models with increasingly flattened outer parts.

Our main conclusions are as follows.

(i) The kinematic data for NGC 3379 out to  $7R_e$  are consistent with a variety of potentials and do not give strong constraints on the mass distribution in this galaxy. The main reason for this is the well-known degeneracy between mass and radial anisotropy which is substantial when the velocity dispersion profile falls with radius. Formal confidence limits on the halo circular velocity at  $7R_e$  are  $165 \text{ km s}^{-1} \lesssim v_{\text{circ}}(7R_e) \lesssim 250 \text{ km s}^{-1}$  at  $1\sigma$ , which would weakly exclude models without DM.

(ii) This result appears to be essentially independent of the shape of the luminous mass distribution, pointing towards a shape degeneracy in addition to the well-known mass-anisotropy degeneracy.

(iii) NGC 3379 may well have the kind of DM halo consistent with the current  $\Lambda$ CDM paradigm. The circular velocity curves of the merger models constructed by Dekel et al. (2005) in the  $\Lambda$ CDM cosmology framework,  $v_{\text{circ}}(r)/v_{\text{circ}}(R_e) \simeq (R/R_e)^{-0.135}$ , fall right into the range of circular velocities of our best-fitting models in Fig. 11.

(iv) Such models, however, are required by the data to have strongly radially anisotropic orbit distributions in their outer regions,  $\beta \gtrsim 0.8$  at  $7R_e$ , while model predictions at  $7R_e$  are  $0.3 \lesssim \beta \lesssim 0.6$  (Dekel et al. 2005) and  $\beta \simeq 0.7$  (Abadi, Navarro & Steinmetz 2006). Kinematic data at even larger radii than presently available would be required to discriminate between these models and less anisotropic models with lower mass haloes.

## ACKNOWLEDGMENTS

We thank John Magorrian for making his software available, Jens Thomas for helpful advice and discussions and the referee for careful readings of the manuscript.

## REFERENCES

Abadi M. G., Navarro J. F., Steinmetz M., 2006, *MNRAS*, 365, 747  
 Awaki H. et al., 1994, *PASJ*, 46, L65  
 Binney J., Mamon G. A., 1982, *MNRAS*, 200, 361  
 Binney J., Tremaine S., 1987, *Galactic Dynamics*. Princeton Univ. Press, Princeton, NJ  
 Bissantz N., Debattista V. P., Gerhard O., 2004, *ApJ*, 601, L155  
 Capaccioli M., Held E. V., Lorenz H., Vietri M., 1990, *AJ*, 99, 1813  
 Capaccioli M., Vietri M., Held E. V., Lorenz H., 1991, *ApJ*, 371, 535  
 Cappellari M. et al., 2006, *MNRAS*, 366, 1126  
 Carollo C. M., de Zeeuw P. T., van der Marel R. P., 1995, *MNRAS*, 276, 1131  
 Chanamé J., Kleyna J., van der Marel R., 2008, *ApJ*, 682, 841  
 Coccatto L. et al., 2009, *MNRAS*, 394, 1249  
 Cretton N., de Zeeuw P. T., van der Marel R. P., Rix H.-W., 1999, *ApJS*, 124, 383

de Lorenzi F., Debattista V. P., Gerhard O. E., 2006, in Stanghellini L., Walsh J. R., Douglas N. G., eds, *Planetary Nebulae Beyond the Milky Way*. Springer, Berlin, p. 311  
 de Lorenzi F., Debattista V. P., Gerhard O., Sambhus N., 2007, *MNRAS*, 376, 71  
 de Lorenzi F., Gerhard O., Saglia R. P., Sambhus N., Debattista V. P., Pannella M., Méndez R. H., 2008, *MNRAS*, 385, 1729  
 Debattista V. P., Sellwood J. A., 2000, *ApJ*, 543, 704  
 Dekel A., Stoehr F., Mamon G. A., Cox T. J., Novak G. S., Primack J. R., 2005, *Nat*, 437, 707  
 Douglas N. G. et al., 2002, *PASP*, 114, 1234  
 Douglas N. G. et al., 2007, *ApJ*, 664, 257  
 Dubinski J., Carlberg R. G., 1991, *ApJ*, 378, 496  
 Franx M., van Gorkom J. H., de Zeeuw T., 1994, *ApJ*, 436, 642  
 Fukazawa Y., Botoya-Nonesca J. G., Pu J., Ohto A., Kawano N., 2006, *ApJ*, 636, 698  
 Gavazzi R., Treu T., Rhodes J. D., Koopmans L. V. E., Bolton A. S., Burles S., Massey R. J., Moustakas L. A., 2007, *ApJ*, 667, 176  
 Gebhardt K. et al., 2000, *AJ*, 119, 1157  
 Gebhardt K. et al., 2003, *ApJ*, 583, 92  
 Gerhard O. E., 1983a, *MNRAS*, 202, 1159  
 Gerhard O. E., 1983b, *MNRAS*, 203, 19  
 Gerhard O. E., 1993, *MNRAS*, 265, 213  
 Gerhard O. E., Binney J. J., 1996, *MNRAS*, 279, 993  
 Gerhard O., Jeske G., Saglia R. P., Bender R., 1998, *MNRAS*, 295, 197  
 Gerhard O., Kronawitter A., Saglia R. P., Bender R., 2001, *AJ*, 121, 1936  
 Hernquist L., 1990, *ApJ*, 356, 359  
 Humphrey P. J., Buote D. A., Gastaldello F., Zappacosta L., Bullock J. S., Brighenti F., Mathews W. G., 2006, *ApJ*, 646, 899  
 Jensen J. B., Tonry J. L., Barris B. J., Thompson R. I., Liu M. C., Rieke M. J., Ajhar E. A., Blakeslee J. P., 2003, *ApJ*, 583, 712  
 Jourdeuil E., Emsellem E., 2007, in Kissler-Patig M., Walsh J. R., Roth M. M., eds, *Science Perspectives for 3D Spectroscopy*. Springer-Verlag, Berlin, p. 99  
 Koopmans L. V. E., Treu T., Bolton A. S., Burles S., Moustakas L. A., 2006, *ApJ*, 649, 599  
 Kronawitter A., Saglia R. P., Gerhard O., Bender R., 2000, *A&AS*, 144, 53  
 Loewenstein M., White R. E., III, 1999, *ApJ*, 518, 50  
 Magorrian J., 1999, *MNRAS*, 302, 530  
 Matsushita K., Makishima K., Ikebe Y., Rokutanda E., Yamasaki N., Ohashi T., 1998, *ApJ*, 499, L13  
 Méndez R. H., Riffeser A., Kudritzki R.-P., Matthias M., Freeman K. C., Arnaboldi M., Capaccioli M., Gerhard O. E., 2001, *ApJ*, 563, 135  
 Merrett H. R. et al., 2003, *MNRAS*, 346, L62  
 Merritt D., 1985, *AJ*, 90, 1027  
 Napolitano N. R. et al., 2005, *MNRAS*, 357, 691  
 Oosterloo T. A., Morganti R., Sadler E. M., Vergani D., Caldwell N., 2002, *AJ*, 123, 729  
 Osipkov L. P., 1979, *PAZh*, 5, 77  
 Rix H.-W., de Zeeuw P. T., Cretton N., van der Marel R. P., Carollo C. M., 1997, *ApJ*, 488, 702  
 Romanowsky A. J., Kochanek C. S., 1997, *MNRAS*, 287, 35  
 Romanowsky A. J., Kochanek C. S., 2001, *ApJ*, 553, 722  
 Romanowsky A. J., Douglas N. G., Arnaboldi M., Kuijken K., Merrifield M. R., Napolitano N. R., Capaccioli M., Freeman K. C., 2003, *Sci*, 301, 1696  
 Rusin D., Kochanek C. S., 2005, *ApJ*, 623, 666  
 Rybicki G. B., 1987, in de Zeeuw P. T., ed., *Proc. IAU Symp. 127, Structure and Dynamics of Elliptical Galaxies*. Reidel, Dordrecht, p. 397  
 Schwarzschild M., 1979, *ApJ*, 232, 236  
 Sellwood J. A., 2003, *ApJ*, 587, 638  
 Sersic J. L., 1968, *Atlas de Galaxias Australes*. Observatorio Astronomico, Cordoba, Argentina  
 Shapero K. L., Cappellari M., de Zeeuw T., McDermid R. M., Gebhardt K., van den Bosch R. C. E., Statler T. S., 2006, *MNRAS*, 370, 559  
 Statler T. S., 2001, *AJ*, 121, 244

- Statler T. S., Smecker-Hane T., 1999, *AJ*, 117, 839  
Syer D., Tremaine S., 1996, *MNRAS*, 282, 223  
Thomas J., 2006, PhD thesis, Ludwig–Maximilians–Universität München  
Thomas J., Saglia R. P., Bender R., Thomas D., Gebhardt K., Magorrian J., Richstone D., 2004, *MNRAS*, 353, 391  
Thomas J., Saglia R. P., Bender R., Thomas D., Gebhardt K., Magorrian J., Corsini E. M., Wegner G., 2005, *MNRAS*, 360, 1355  
Thomas J., Saglia R. P., Bender R., Thomas D., Gebhardt K., Magorrian J., Corsini E. M., Wegner G., 2007, *MNRAS*, 382, 657  
Treu T., Koopmans L. V. E., 2004, *ApJ*, 611, 739  
Valluri M., Merritt D., Emsellem E., 2004, *ApJ*, 602, 66  
van den Bosch R. C. E., van de Ven G., Verolme E. K., Cappellari M., de Zeeuw P. T., 2008, *MNRAS*, 385, 647  
van der Marel R. P., Franx M., 1993, *ApJ*, 407, 525  
van der Marel R. P., Cretton N., de Zeeuw P. T., Rix H.-W., 1998, *ApJ*, 493, 613  
Wilson G., Kaiser N., Luppino G. A., Cowie L. L., 2001, *ApJ*, 555, 572

This paper has been typeset from a  $\text{\TeX/L\TeX}$  file prepared by the author.